

Photometry and Spectroscopy of Faint Candidate Spectrophotometric Standard DA White Dwarfs

Annalisa Calamida^{1,2}, Thomas Matheson¹, Abhijit Saha¹, Edward Olszewski³, Gautham Narayan^{1,2}, Jenna Claver¹, Clare Shanahan², Jay Holberg⁴, Tim Axelrod³, Ralph Bohlin², Christopher W. Stubbs⁵, Susana Deustua², Ivan Hubeny³, John Mackenty², Sean Points⁶, Armin Rest^{2,7}, and Elena Sabbi², National Optical Astronomy Observatory—AURA, 950 N Cherry Avenue, Tucson, AZ 85719, USA; calamida@stsci.edu

Space Telescope Science Institute—AURA, 3700 San Martin Drive, Baltimore, MD 21218, USA

Steward Observatory, University of Arizona, 933 N Cherry Avenue, Tucson, AZ 85719, USA

Lunar and Planetary Laboratory, University of Arizona, 1629 E University Boulevard, Tucson, AZ 85721, USA

Harvard University, 17 Oxford Street, Cambridge, MA 02138, USA

Cerro Tololo Inter-American Observatory, Casilla 603, La Serena, Chile

Department of Physics and Astronomy, Johns Hopkins University, Baltimore, MD 21218, USA

Received 2018 November 13; revised 2018 December 22; accepted 2018 December 23; published 2019 February 25

Abstract

We present precise photometry and spectroscopy for 23 candidate spectrophotometric standard white dwarfs. The selected stars are distributed in the Northern hemisphere and around the celestial equator, and are all fainter than $r \sim 16.5$ mag. This network of stars, when established as standards and together with the three *Hubble Space Telescope* primary CALSPEC white dwarfs, will provide a set of spectrophotometric standards to directly calibrate data products to better than 1%. In future deep photometric surveys and facilities, these new faint standard white dwarfs will have enough signal-to-noise ratio to be measured accurately while still avoiding saturation. They will also fall within the dynamic range of large telescopes and their instruments for the foreseeable future. This paper discusses the provenance of the observational data for our candidate standard stars. A comparison with models, reconciliation with reddening, and the consequent derivation of the full spectral energy density distributions for each of them is reserved for a subsequent paper.

Key words: methods: observational – standards – stars: fundamental parameters – techniques: photometric – techniques: spectroscopic – white dwarfs

Supporting material: machine-readable tables

1. Introduction

Astrophysics is at the threshold of an era of deep imaging surveys of large portions of the sky, both from the ground and from telescopes in space. Projects such as the Sloan Digital Sky Survey (SDSS), Pan-STARRS (PS), the Dark Energy Survey (DES), Skymapper, the Asteroid Terrestrial-impact Last Alert System (ATLAS), the All Sky Automated Survey for Super-Novae (ASAS-SN), the Galaxy Evolution Explorer (GALEX), and the Wide-field Infrared Survey Explorer (WISE) are either complete or in their advanced stages, while the Zwicky Transient Facility (ZTF) has just begun and the Large Synoptic Survey Telescope (LSST) is only a few years away. 8 GAIA and Kepler continue to report photometry of millions of stars to very high internal accuracy. These projects have their own native pass-bands and photometric systems, some of which are similar while others differ significantly. To make the information across these projects commensurate with each other, we must put them on a common photometric system. Therefore, we need a set of calibration references, with which both existing and future surveys can be cross-calibrated. Specifically, we seek to establish a set of standard stars that satisfy the following criteria:

1. They must have relative spectral energy distributions (SEDs) that are established to sub-percent accuracy, and preferably to better than half-percent.

- 2. They must fall within the dynamic range of most, if not all, extant and future deep surveys. We surmise that these stars should be fainter than $r \sim 16.5$ mag, which also puts them within the dynamic range of large large-aperture telescopes.
- 3. They must be distributed across the sky so that they are naturally observed in past, present and future surveys, making it possible to retroactively re-calibrate photometry onto a common (spectro)-photometric scale. This will allow the direct collation of photometry from different surveys with their own respective native passbands onto a commensurate platform. For other investigations, a few of the standards will always be available from any observatory at any point in time.

Sub-percent global photometric standardization has proven challenging in the past but is in high demand for several ongoing scientific endeavors. It is also the major source of uncertainty in the use of Type Ia supernovae as probes of the history of cosmic expansion to infer the properties of dark energy (Betoule et al. 2014; Scolnic et al. 2015; Stubbs & Brown 2015). Experiments that require accurate and reliable photoredshift determination, such as weak lensing tomography and baryonic acoustic oscillation analysis with LSST (Gorecki et al. 2014), are also limited by systematic uncertainties arising from their relative photometric calibration.

The chief obstacle for calibrating standard stars with high accuracy from the ground by comparing them to laboratory sources is the uncertainty in atmospheric extinction. Ground-based

⁸ Table 10 in the Appendix lists and describes all the acronyms used in the manuscript.

survey accuracy is limited by the transmissivity of the atmosphere, with both chromatic (Rayleigh scattering, ozone, Mie scattering, molecular absorption, aerosol) and gray (clouds) terms varying on small angular and temporal scales. A variety of methods are used to track and account for these effects, including monitoring (e.g., LIDAR, GPS). Many efforts are also made to model the atmosphere (e.g., with MODTRAN, Burke et al. 2014). Although it would be ideal to place laboratory sources above the terrestrial atmosphere, this is unlikely to happen in the near future. For a more detailed discussion of the problems related to obtaining a sub-percent accurate calibration, please see Narayan et al. (2016, hereafter NA16).

Therefore, we seek extra-terrestrial sources for which we can predict the SED to higher accuracy than the uncertainty in predicting the transmissivity of the terrestrial atmosphere. The best class of celestial objects that we can hope to characterize and model are hot DA white dwarfs (DAWDs). These stars have almost pure-hydrogen atmospheres, which makes them the simplest stellar atmospheres to model. In addition, their opacities are known from first principles, at temperatures greater than $\sim\!20,000\,\mathrm{K}$ the photospheres are purely radiative, and they are photometrically stable.

The intrinsic DAWD SED can be described by two parameters: effective temperature, $T_{\rm eff}$, and surface gravity, $\log(g)$. Both of these parameters can be measured spectroscopically from a detailed analysis of the Balmer line profiles, without using photometry. The SED can then be modeled from the ultraviolet (UV) to the near-infrared and projected through the transmission of any imager or spectrometer at arbitrary resolution. Only the extinction toward the observed DAWDs and the overall flux normalization need to be established.

Bohlin (2000) and Bohlin et al. (2014, hereafter B14) implemented the pure-hydrogen-WD method of flux calibration using three DAWDs—G191B2B, GD153 and GD71 (Hubble Space Telescope (HST) primary WDs). These stars are brighter than $V \sim 13.5$ mag, they span a range of temperatures $30,000 \lesssim T_{\rm eff} \lesssim 60,000$, and they are un-reddened as a result of their proximity to us. B14 found their relative flux distributions to be internally consistent with the model predictions (Gianninas et al. 2011; Rauch et al. 2013) from spectroscopic $T_{\rm eff}$ and $\log g$ to better than 1% in the wavelength range 0.2–0.9 μ m. Spectrophotometry of Vega with STIS (Bohlin & Gilliland 2004; Bohlin 2007) referred to the DAWD flux scale shows agreement with Hayes et al.'s (1985) calibration at the 1%–2% level, and with the Kurucz Vega atmosphere model to better than 1% in the wavelength range $0.5-0.8 \mu m$, but disagrees by 5% at $0.4 \mu m$, and by 10% between 0.9 and 1.0 μ m. This illustrates the limitation of empirical ground-based methods.

The internal consistency of the DAWD observations and models (≤ 5 mmag) in the wavelength range 0.2–0.9 μ m is superior to the $\sim 2\%$ comparison with the best model for Vega (Kurucz at $T_{\rm eff} = 9400$ K), which is a pole-on rapid rotator with an equatorial dust disk. The zero-point (ZP) for the *HST* photometric system is defined by the flux of 3.44 \times 10⁻⁹ erg cm⁻² s⁻¹ Å⁻¹ for Vega at 0.5556 μ m, as reconciled with the *Midcourse Space Experiment (MSX)* mid-IR absolute flux measures (B14, and Bohlin 2014). Absolute fluxes for the three *HST* primary WDs are determined by the normalization of their modeled SEDs by their respective relative responses to

Holberg & Bergeron (2006) used synthetic photometry of DAWDs in the magnitude range $10 \lesssim V \lesssim 16.5$ to place *UBVRI*, 2MASS *JHK*, SDSS *ugriz* and Strömgren *ubvy* magnitudes on the *HST* photometric scale to 1%. Later, Holberg et al. (2008) confirmed this calibration by using a set of DAWDs in the same magnitude range with well-measured trigonometric parallaxes that agreed at the 1% level with their photometric parallaxes from the Bergeron photometric grid. However, the DAWDs in use to date are still too bright for modern deep surveys and large telescopes.

To provide flux standards in the dynamic range of large-aperture (d>4 m) telescopes, we obtained Wide-Field Camera 3 (WFC3) HST imaging and ground-based spectroscopy for the three HST primary (CALSPEC) standards—G191B2B, GD153, and GD71—along with 23 DAWDs fainter than $r\sim16.5$ mag, at equatorial and northern latitudes. The need for practical faint standards, which are useful over the optical and near-UV, makes consideration of the effects of interstellar extinction unavoidable. Indeed, interstellar medium extinction must be incorporated into the definition of the SEDs of all faint flux standards. Fortunately, as sub-luminous stars, DAWDs are the optimal choice because they simultaneously offer minimal extinction columns and wide wavelength coverage, from the far-UV to the IR.

The current paper presents our analysis of photometric and spectroscopic data collected for the candidate spectrophotometric DAWDs. The preliminary results of the temporal photometric monitoring campaign of the DAWDs are also presented. Photometric and spectroscopic data are examined to determine the suitability of each of the 23 candidates as SED standards. The joint analysis of photometry and spectroscopy and the derivation of SEDs and reddening to each of these objects are reserved for a subsequent paper (Narayan et al. 2019, hereafter NA19).

The structure of the current paper is as follows. In Section 2, we discuss the criteria used to select candidate spectro-photometric standard DAWDs and in Section 3 we illustrate the photometric observations and the image processing strategy. In Section 4, we describe the photometric reduction procedures and in Section 5 the stability monitoring observations for the candidate standards. In Section 6, the spectroscopic data reduction strategy is described and in Section 7 we discuss how our photometry is calibrated and normalized. We summarize our results in Section 8.

2. Candidate Spectrophotometric Standard Star Selection

Candidate spectrophotometric standard DAWDs were selected from the SDSS (Adelman-McCarthy et al. 2008; Girven et al. 2012; Kleinman et al. 2013) and the Villanova catalog (McCook & Sion 1999), with the requirement of being spectral type DA, hotter than $\approx\!20,\!000\,\text{K},$ and fainter than r $\sim\!16.5\,\text{mag}.$ We selected an adequate number of stars to uniformly cover the sky around the celestial equator and in the Northern hemisphere. The final sample consists of 23 candidate standard DAWDs. Table 1 lists the properties of the selected

Vega, using STIS precision spectrophotometry of all four stars —Vega, G191B2B, GD153 and GD71—and the 3.44 \times $10^{-9}~\rm erg~cm^{-2}~s^{-1}~\mathring{A}^{-1}$ flux of Vega at 0.5556 μm . This method provides the basis for HST's entire calibration system (CALSPEC 10).

⁹ http://kurucz.harvard.edu/stars/vega/

¹⁰ http://www.stsci.edu/hst/observatory/crds/calspec.html

Table 1 List of Properties of the HST Primary CALSPEC Standards and the 23 Candidate Spectrophotometric Standard DAWDs

Star	Alt Name	R.A. ^a (hh:mm:ss.s)	Decl. ^a (dd:mm:ss.s)	PM _{R.A.} a (mas yr ⁻¹)	PM _{Decl.} ^a (mas yr ⁻¹)	SType ^a	Distance ^a (pc)	T _{eff} ^b (K)	$\log(g)^{\mathbf{b}}$
G191B2B	BD+52 913	5:05:30.613	52:49:51.956	12.592 ± 0.122	-93.525 ± 0.106	DA.89	52.9 ± 0.2	57340	7.48
GD71	GD71	5:52:27.614	15:53:13.751	76.841 ± 0.131	-172.944 ± 0.104	DA1.5	51.9 ± 0.2	32780	7.83
GD153	GD153	12:57:02.337	22:01:52.68	-38.410 ± 0.119	-202.953 ± 0.116	DA1.3	68.6 ± 0.3	39390	7.77
SDSSJ010322.19-002047.7	SDSSJ010322.19-002047.7	1:03:22.191	-0:20:47.731	6.216 ± 0.957	-6.313 ± 0.549	DA.67	1097 ± 611	75000	7.81
SDSSJ022817.16-082716.4	WD0225-086	2:28:17.169	-8:27:16.409	12.241 ± 1.461	3.827 ± 1.000	DA2.45	525 ± 181	20555	7.87
SDSSJ024854.96+334548.3	SDSSJ024854.96+334548.3	2:48:54.967	33:45:48.33	3.635 ± 0.700	-4.718 ± 0.442	DA1.46	630 ± 128	34497	7.30
SDSSJ041053.632-063027.580	WD0408-066	4:10:53.634	-6:30:27.749	8.620 ± 0.411	9.700 ± 0.237	DA.77	1833 ± 1248	65796	7.52
WD0554-165	WD0554-165	5:57:01.296	-16:35:12.12	-7.188 ± 0.399	4.781 ± 0.623		239 ± 13		
SDSSJ072752.76+321416.1	SDSSJ072752.76+321416.1	7:27:52.76	32:14:16.141	-13.095 ± 0.366	-7.094 ± 0.373	DA.88	990 ± 198	57865	7.61
SDSSJ081508.78+073145.7	SDSSJ081508.78+073145.7	8:15:08.779	7:31:45.804	3.135 ± 1.384	0.313 ± 0.794	DA1.55		32387	6.81
SDSSJ102430.93-003207.0	SDSSJ102430.93-003207.0	10:24:30.932	-0.32:07.03	-24.0	-5.0	DA1.21		41584	7.77
SDSSJ111059.42-170954.2	SDSSJ111059.42-170954.2	11:10:59.428	-17:09:54.27	5.045 ± 0.418	-7.763 ± 0.293	DA.96	1333 ± 359	52555	7.73
SDSSJ111127.30+395628.0	SDSSJ111127.30+395628.0	11:11:27.309	39:56:28.079	3.277 ± 0.445	3.095 ± 0.598	DA.75	648 ± 166	67380	7.80
SDSSJ120650.504+020143.810	WD1204+023	12:06:50.408	2:01:42.46	-4.594 ± 0.663	-23.143 ± 0.319	DA2.02	590 ± 130	24926	7.98
SDSSJ121405.11+453818.5	CSO1291	12:14:05.112	45:38:18.56	0.291 ± 0.140	13.803 ± 0.170	DA1.43	495 ± 31	35245	7.91
SDSSJ130234.43+101238.9	SDSSJ130234.43+101238.9	13:02:34.441	10:12:39.01	-12.523 ± 0.252	-17.372 ± 0.191	DA1.20	389 ± 17	42070	7.91
SDSSJ131445.050-031415.588	WD1312-029	13:14:45.05	-3:14:15.641	-4.102 ± 1.190	-6.354 ± 0.606	DA1.05	1154 ± 834	47818	7.76
SDSSJ151421.27+004752.8	LB 769	15:14:21.28	0:47:52.883	4.400 ± 0.175	-27.041 ± 0.222	DA1.74	157 ± 3	28999	7.81
SDSSJ155745.40+554609.7	WD1556+559	15:57:45.404	55:46:09.75	-11.545 ± 0.260	-21.340 ± 0.204	DA.79	$688 \pm 52.$	64122	7.65
SDSSJ163800.360+004717.822	WD1635+008	16:38:00.366	0:47:17.801	-9.582 ± 0.782	-2.797 ± 0.467	DA.77	876 ± 283	65116	7.37
SDSSJ172135.97+294016.0	SDSSJ172135.97+294016.0	17:21:35.981	29:40:15.996	-21.454 ± 0.564	10.452 ± 0.638	DA5.44	271 ± 26	9261	8.33
SDSSJ181424.075+785403.048	WD1817+788	18:14:24.122	78:54:02.909	-11.041 ± 0.103	11.292 ± 0.132	DA1.6	257 ± 3	31500	7.81
SDSSJ20372.169-051302.964	WD2034-053	20:37:22.167	-5:13:03.029	3.106 ± 0.647	-2.723 ± 0.389	DA1.33	912 ± 324	37923	7.92
SDSSJ210150.65-054550.9	WD2059-059	21:01:50.657	-5:45:50.969	10.828 ± 0.456	-11.727 ± 0.372	DA1.75	662 ± 107	28816	7.78
SDSSJ232941.330+001107.755	WD2327-000	23:29:41.325	0:11:07.8	-8.299 ± 0.384	-14.421 ± 0.277	DA2.37	318 ± 25	21266	7.88
SDSSJ235144.29+375542.6	SDSSJ235144.29+375542.6	23:51:44.293	37:55:42.661	-16.575 ± 0.294	-10.048 ± 0.185	DA.95	765 ± 134	53333	7.72

Notes.

^a Coordinates, proper motions, spectral type, and distance measurements are from *GAIA* DR2.

^b Effective temperature and surface gravity measurements are from the SDSS or the Villanova catalogs.

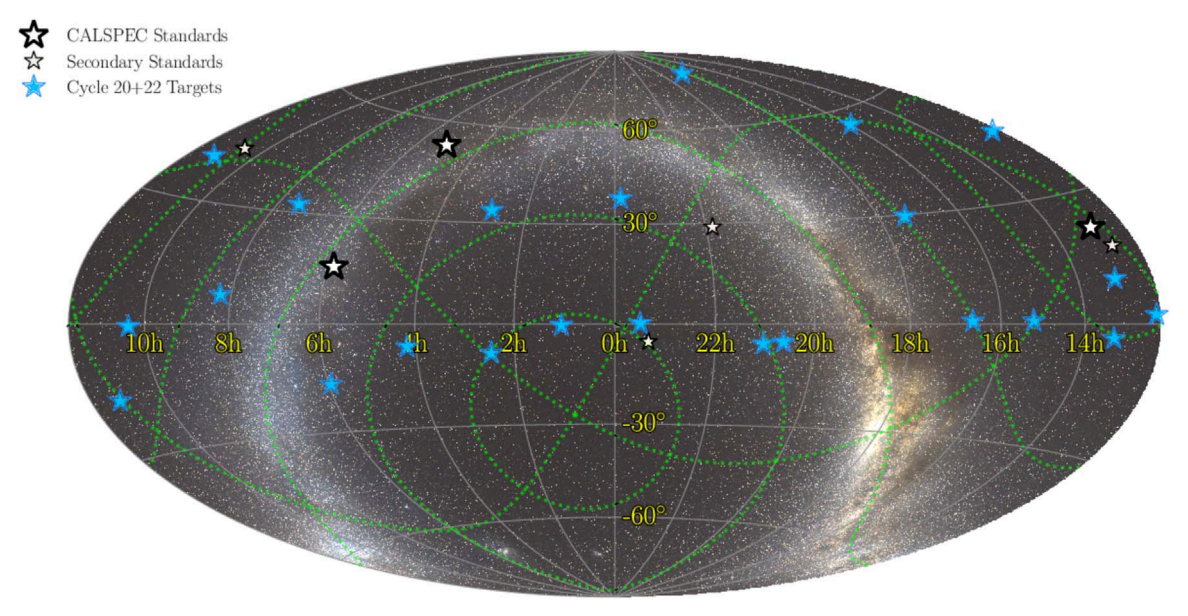


Figure 1. A Hammer–Aitoff projection of the 23 candidate spectrophotometric standard DAWDs observed with *HST* in cycles 20 and 22 in equatorial coordinates (blue stars). The three *HST* primary CALSPEC standards are marked with a large white star and four spectroscopic flux standards (secondary standards) are marked with a small white star.

stars and the three *HST* primary CALSPEC standards (GD71, GD153, G191B2B), including spectral type, proper motions and distances from the *GAIA* data release 2 (DR2, Gaia Collaboration et al. 2018).

Figure 1 shows a Hammer–Aitoff projection of the sky with the distribution of the *HST* primary (CALSPEC) standard WDs (large white stars) and the 23 selected candidate standard DAWDs (blue). The four secondary flux standard stars that are used to calibrate spectra analyzed in the current paper are also shown in the figure as small white stars. The figure shows that candidate standards have an homogeneous coverage over the Northern hemisphere and the celestial equator, with approximately 1 star every 2 hr.

We have a sample of candidate DAWDs for the Southern hemisphere, for which spectra collected with the Goodman spectrograph on the SOAR telescope (CTIO) are available and *HST* photometry was collected during Cycle 25 (GO-15113, PI: Saha). A subsequent paper will present photometry and spectroscopy for these new candidates. The final goal is to provide an all-sky set of sub-percent precision spectrophotometric standards so that at least three of these stars are visible at any time from any observatory at an airmass less than 2.

Preliminary effective temperatures and gravities to select candidate spectrophotometric standards were retrieved from the SDSS and the Villanova catalogs. The ground-based spectra that we collected using different facilities will be used to derive more accurate temperatures and gravities for all the DAWDs, as described in Section 6. The HST primary WDs and the candidate standards are plotted in the T_{eff} versus $\log(g)$ plane in Figure 2. For star WD0554–165, T_{eff} and $\log(g)$ measurements are unavailable in the literature. The figure shows that star SDSS-J172135.97+294016.0 is much cooler compared to the other DAWDs, with an effective temperature of $T_{\rm eff} = 9261 \, {\rm K}$ (see Table 1). This star was included in the sample because of an early decision that was made before we restricted ourselves to purely radiative atmospheres with temperatures $T_{\rm eff} > 20,000 \, {\rm K}$. Although the observations and data reduction for this star were carried through, this object will no longer be included in the network of standard DAWDs.

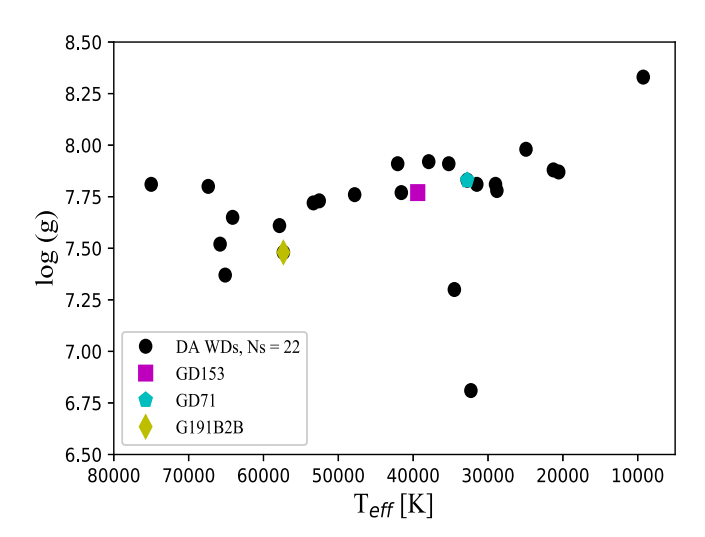


Figure 2. $T_{\rm eff}$ vs. $\log(g)$ plane for 22 selected DA white dwarfs (black dots) and the three *HST* primary CALSPEC standards: G191B2B (yellow diamond), GD153 (magenta square), and GD71 (cyan pentagon).

We matched the list of candidates with PS Data Release 1 catalog (Chambers et al. 2016; Flewelling et al. 2016) and obtained *g*, *r*, *i*, *z* aperture photometry magnitudes for all of these stars. These data will be later used to check the the stellar density around the candidate standards. We also retrieved *GAIA* DR2 *G*, *Bp*, *Rp* magnitudes for the DAWDs. PS and *GAIA* sets of magnitudes are listed in Tables 2 and 3, respectively.

Figure 3 shows the Bp-Rp, F475W – F775W color–color diagram for the 23 candidate standard DAWDs (black dots) and the three primary standards: G191B2B (yellow diamond), GD153 (magenta square) and GD71 (cyan pentagon). The photometry in the HST filters is from this work (see Section 7 and Table 9). The selected candidate standards and the primary HST WDs cluster along a well-defined sequence and have colors in the range $-0.6 \lesssim Bp-Rp \lesssim -0.1$ and $-0.4 \lesssim F475W-F775W \lesssim 0$ mag, excluding star SDSSJ172135.97 +294016.0, $\sim 0.3-0.4$ mag redder than the rest of the WDs,

 Table 2

 Pan-STARRS1 Photometry for the Candidate Spectrophotometric Standard DA White Dwarfs

Star	R.A. (hh:mm:ss.s)	Decl. (dd:mm:ss.s)	g (mag)	err _g (mag)	r (mag)	err _r (mag)	i (mag)	err _i (mag)	z (mag)	err _z (mag)
G191B2B	5:05:30.613	52:49:51.956								
GD71	5:52:27.614	15:53:13.751	12.846	0.003	13.284	0.001	13.629	0.005	13.921	0.003
GD153	12:57:02.337	22:01:52.68	13.115	0.004	13.586	0.001	13.968	0.006	14.257	0.002
SDSSJ010322.19-002047.7	1:03:22.191	-0:20:47.731	19.093	0.010	19.570	0.019	19.979	0.017	20.130	0.064
SDSSJ022817.16-082716.4	2:28:17.169	-8:27:16.409	19.837	0.014	20.188	0.053	20.523	0.036	20.803	0.117
SDSSJ024854.96+334548.3	2:48:54.967	33:45:48.33	18.351	0.007	18.699	0.006	18.972	0.012	19.198	0.031
SDSSJ041053.632-063027.580	4:10:53.634	-6:30:27.749	18.871	0.008	19.224	0.010	19.429	0.022	19.342	0.028
WD0554-165	5:57:01.296	-16:35:12.12	17.787	0.012	18.237	0.012	18.628	0.010	18.916	0.010
SDSSJ072752.76+321416.1	7:27:52.76	32:14:16.141	18.018	0.010	18.475	0.011	18.806	0.012	19.127	0.024
SDSSJ081508.78+073145.7	8:15:08.779	7:31:45.804	19.781	0.040	20.328	0.037	20.625	0.073	20.710	0.165
SDSSJ102430.93-003207.0	10:24:30.932	-0:32:07.03	18.885	0.009	19.292	0.023	19.440	0.098	19.758	0.031
SDSSJ111059.42-170954.2	11:10:59.428	-17:09:54.27	17.895	0.005	18.302	0.009	18.607	0.015	18.957	0.026
SDSSJ111127.30+395628.0	11:11:27.309	39:56:28.079	18.412	0.015	18.886	0.011	19.260	0.011	19.586	0.016
SDSSJ120650.504+020143.810	12:06:50.408	2:01:42.46	18.693	0.010	19.096	0.029	19.388	0.024	19.645	0.034
SDSSJ121405.11+453818.5	12:14:05.112	45:38:18.56	17.779	0.005	18.236	0.007	18.570	0.010	18.849	0.017
SDSSJ130234.43+101238.9	13:02:34.441	10:12:39.01	17.052	0.003	17.494	0.003	17.858	0.006	18.114	0.009
SDSSJ131445.050-031415.588	13:14:45.05	-3:14:15.641	19.078	0.014	19.556	0.021	19.887	0.040	20.240	0.069
SDSSJ151421.27+004752.8	15:14:21.28	0:47:52.883	15.720	0.002	16.101	0.004	16.434	0.002	16.715	0.005
SDSSJ155745.40+554609.7	15:57:45.404	55:46:09.75	17.487	0.005	17.958	0.007	18.356	0.005	18.647	0.011
SDSSJ163800.360+004717.822	16:38:00.366	0:47:17.801	18.860	0.013	19.314	0.022	19.611	0.013	19.816	0.053
SDSSJ172135.97+294016.0	17:21:35.981	29:40:15.996	19.637	0.015	19.636	0.015	19.754	0.024	19.995	0.101
SDSSJ181424.075+785403.048	18:14:24.122	78:54:02.909	16.573	0.005	17.007	0.003	17.358	0.004	17.651	0.009
SDSSJ20372.169-051302.964	20:37:22.167	-5:13:03.029	18.987	0.009	19.349	0.010	19.576	0.020	19.881	0.047
SDSSJ210150.65-054550.9	21:01:50.657	-5:45:50.969	18.652	0.009	19.052	0.008	19.410	0.018	19.703	0.033
SDSSJ232941.330+001107.755	23:29:41.325	0:11:07.8	18.134	0.006	18.452	0.005	18.772	0.008	19.003	0.017
SDSSJ235144.29+375542.6	23:51:44.293	37:55:42.661	18.085	0.004	18.447	0.013	18.776	0.010	19.100	0.036

 ${\bf Table~3} \\ {\it GAIA~DR2~Photometry~for~the~Candidate~Spectrophotometric~Standard~DA~White~Dwarfs}$

Star	R.A.	Decl.	G	err_G	Rp	err_{Rp}	Вр	err _{Bp}
	(hh:mm:ss.s)	(dd:mm:ss.s)	(mag)	(mag)	(mag)	(mag)	(mag)	(mag)
G191B2B	5:05:30.613	52:49:51.956	11.738	0.001	12.067	0.002	11.487	0.015
GD71	5:52:27.614	15:53:13.751	13.026	0.002	13.299	0.002	12.77	0.012
GD153	12:57:02.337	22:01:52.68	13.322	0.0	13.629	0.001	13.081	0.005
SDSSJ010322.19-002047.7	1:03:22.191	-0:20:47.731	19.356	0.004	19.577	0.072	19.154	0.03
SDSSJ022817.16-082716.4	2:28:17.169	-8:27:16.409	20.046	0.01	20.192	0.141	19.869	0.139
SDSSJ024854.96+334548.3	2:48:54.967	33:45:48.33	18.561	0.003	18.704	0.031	18.333	0.047
SDSSJ041053.632-063027.580	4:10:53.634	-6:30:27.749	19.024	0.002	19.013	0.023	18.861	0.025
WD0554-165	5:57:01.296	-16:35:12.12	17.98	0.003	18.306	0.03	17.726	0.022
SDSSJ072752.76+321416.1	7:27:52.76	32:14:16.141	18.232	0.003	18.458	0.036	17.944	0.007
SDSSJ081508.78+073145.7	8:15:08.779	7:31:45.804	19.996	0.005	20.278	0.166	19.695	0.044
SDSSJ102430.93-003207.0	10:24:30.932	-0.32:07.03	19.12	0.005	19.297	0.105	18.94	0.059
SDSSJ111059.42-170954.2	11:10:59.428	-17:09:54.27	18.089	0.002	18.347	0.02	17.852	0.011
SDSSJ111127.30+395628.0	11:11:27.309	39:56:28.079	18.69	0.003	18.955	0.075	18.365	0.022
SDSSJ120650.504+020143.810	12:06:50.408	2:01:42.46	18.885	0.002	18.957	0.03	18.651	0.017
SDSSJ121405.11+453818.5	12:14:05.112	45:38:18.56	18.002	0.001	18.154	0.038	17.757	0.011
SDSSJ130234.43+101238.9	13:02:34.441	10:12:39.01	17.268	0.001	17.527	0.012	17.044	0.006
SDSSJ131445.050-031415.588	13:14:45.05	-3:14:15.641	19.354	0.004	19.631	0.082	19.082	0.042
SDSSJ151421.27+004752.8	15:14:21.28	0:47:52.883	15.905	0.001	16.119	0.005	15.743	0.009
SDSSJ155745.40+554609.7	15:57:45.404	55:46:09.75	17.721	0.002	18.019	0.018	17.452	0.014
SDSSJ163800.360+004717.822	16:38:00.366	0:47:17.801	19.065	0.002	19.313	0.04	18.853	0.019
SDSSJ172135.97+294016.0	17:21:35.981	29:40:15.996	19.648	0.005	19.528	0.037	19.733	0.042
SDSSJ181424.075+785403.048	18:14:24.122	78:54:02.909	16.773	0.002	17.031	0.007	16.57	0.009
SDSSJ20372.169-051302.964	20:37:22.167	-5:13:03.029	19.148	0.003	19.375	0.055	18.982	0.018
SDSSJ210150.65-054550.9	21:01:50.657	-5:45:50.969	18.867	0.002	19.095	0.044	18.654	0.021
SDSSJ232941.330+001107.755	23:29:41.325	0:11:07.8	18.323	0.002	18.394	0.028	18.187	0.021
SDSSJ235144.29+375542.6	23:51:44.293	37:55:42.661	18.272	0.002	18.417	0.014	18.056	0.016

Table 4
Log of the Observations Collected with the Wide-Field Camera 3 on Board the *Hubble Space Telescope* during Cycles 20 and 22 (Proposal IDs 12967 and 13711, PI: A. Saha)

Star	PID ^a	Image Name	R.A.	Decl.	Filter	Exposure Time	Date Obs.	Time Obs.	Aperture
			(hh:mm:ss.s)	(dd:mm:ss.s)		(s)	MM/DD)	(UT)	
				Cycle 20					
SDSSJ010322.19-002047.7	12967	ibyn01wxq	01:03:22.1	00:20:47.7	F336W	160	2013 Sep 13	21:46:26	UVIS1-FIX
SDSSJ010322.19-002047.7	12967	ibyn01x0q	01:03:22.1	00:20:47.7	F336W	160	2013 Sep 13	21:51:25	UVIS1-FIX
SDSSJ010322.19-002047.7	12967	ibyn01x2q	01:03:22.1	00:20:47.7	F336W	160	2013 Sep 13	23:17:30	UVIS1-FIX
SDSSJ010322.19-002047.7	12967	ibyn01woq	01:03:22.1	00:20:47.7	F475W	120	2013 Sep 14	20:13:32	UVIS1-FIX
SDSSJ010322.19-002047.7	12967	ibyn01xjq	01:03:22.1	00:20:47.7	F475W	160	2013 Sep 14	01:08:35	UVIS1-FIX
SDSSJ010322.19-002047.7	12967	ibyn01xmq	01:03:22.1	00:20:47.7	F475W	160	2013 Sep 14	01:13:33	UVIS1-FIX
SDSSJ010322.19-002047.7	12967	ibyn01wtq	01:03:22.1	00:20:47.7	F625W	350	2013 Sep 13	20:30:47	UVIS1-FIX
SDSSJ010322.19-002047.7	12967	ibyn01x8q	01:03:22.1	00:20:47.7	F625W	355	2013 Sep 13	23:36:41	UVIS1-FIX
SDSSJ010322.19-002047.7	12967	ibyn01wqq	01:03:22.1	00:20:47.7	F775W	605	2013 Sep 13	20:18:08	UVIS1-FIX
SDSSJ010322.19-002047.7	12967	ibyn01x5q	01:03:22.1	00:20:47.7	F775W	680	2013 Sep 13	23:22:47	UVIS1-FIX
SDSSJ010322.19-002047.7	12967	ibyn01wvq	01:03:22.1	00:20:47.7	F160W	499	2013 Sep 14	21:36:26	IR-FIX
SDSSJ010322.19-002047.7	12967	ibyn01xhq	01:03:22.1	00:20:47.7	F160W	499	2013 Sep 14	00:58:35	IR-FIX
SDSSJ041053.632-063027.580	12967	ibyn02lhq	04:10:53.6	-06:30:27.7	F336W	160	2013 Aug 27	22:02:46	UVIS1-FIX

Note.

(This table is available in its entirety in machine-readable form.)

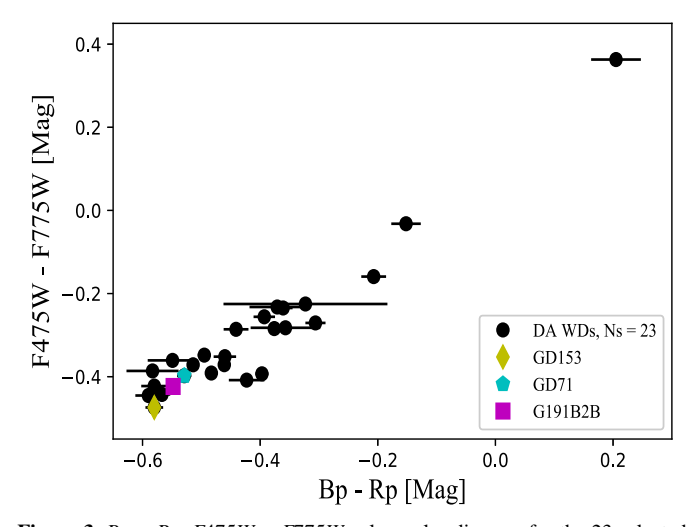


Figure 3. Bp-Rp, F475W-F775W color–color diagram for the 23 selected DA white dwarfs (black dots) and the three HST primary standards: G191B2B (yellow diamond), GD153 (magenta square), and GD71 (cyan pentagon).

which is the cool DAWD included in our sample (as explained previously).

3. Photometric Observations

Photometric data discussed in this investigation were collected with the WFC3 UVIS and IR cameras on board the *HST* during Cycle 20 and 22 (proposals GO-12967 and GO-13711, PI: Saha). Observations were taken in five filters in Cycle 20, namely F336W, F475W, F625W, F775W, F160W. In Cycle 22 the near-UV filter F275W was added to better characterize the line-of sight extinction and the reddening law toward the observed stars.

Nine of the candidate DAWDs are distributed along the celestial equator (hereinafter *equatorial* DAWDs) and were

observed in both Cycle 20 and Cycle 22, while the other 14 DAWDs and the three *HST* primary CALSPEC standards were observed only in Cycle 22. Cycle 20 observations of the nine *equatorial* DAWDs were used in NA16 to demonstrate the effectiveness of our method to establish a network of spectrophotometric standards. We repeated the observations of these stars in Cycle 22 to improve the precision of the photometry. Moreover, photometry of the *equatorial* DAWDs will be used to determine the photometric offset between the two observing cycles. The *HST* primary CALSPEC WDs were observed in Cycle 22 to allow us to directly tie the photometry of the 23 DAWDs to the *HST* photometric system.

Exposure times for our observations range from 1 to $220 \, s$ for the F275W filter, 1 to $160 \, s$ for F336W, 1 to $160 \, s$ for F475W, 1 to $355 \, s$ for F625W, 1 to $680 \, s$ for F775W, and 3 to 499 s for F160W. Table 4 lists the log of the observations for Cycle 20 and 22.

Observations span a time interval of about 1 yr for Cycle 20 (2012 November until 2013 September) and about 1.3 yr for Cycle 22 (2014 September until 2016 January), with the *HST* primary CALSPEC WDs observed at the beginning and the end of Cycle 22 to track the change in sensitivity of the telescope and instrument system.

For the nine *equatorial* DAWDs, three dithered exposures in F336W and F475W, and two exposures for the other filters were collected in Cycle 20. The same targets were observed in Cycle 22 with a cosmic ray (CR) split of 3 exposures for F275W, and one exposure was added for the other filters. In summary, a total of three exposures for each of the WFC3 filters were collected for the nine *equatorial* DAWDs. At least three exposures per filter are needed to check consistency in the photometry at sub-percent precision: WFC3 images are affected by CRs and different detector artifacts, such as hot and bad pixels, blobs, ghosts. As an example, images in six filters for star SDSSJ232941.330+001107.755 are shown in Figure 4. If a star has discrepant measurements in two

^a Program ID.

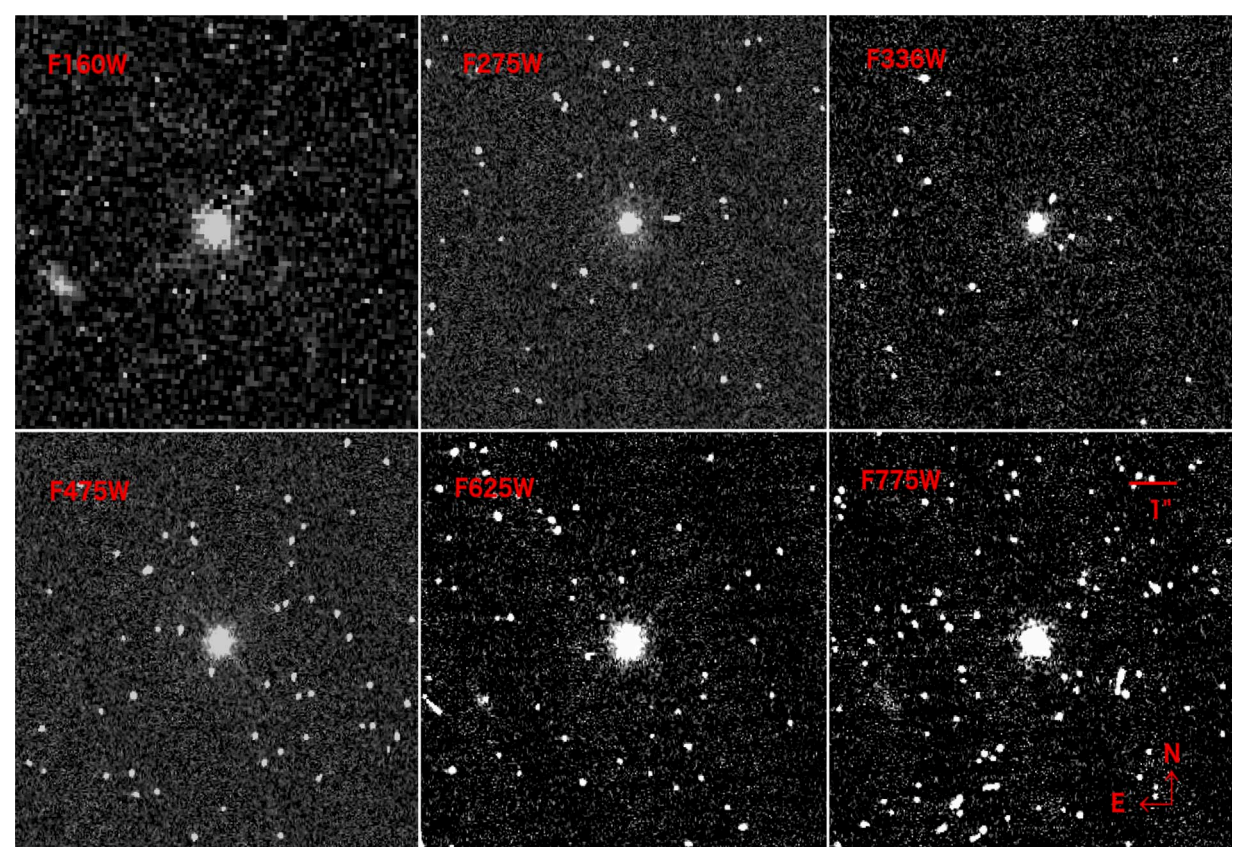


Figure 4. WFC3 FLC images in six filters for the DA white dwarf SDSSJ232941.330+001107.755. The scale of the image and the North and the East directions are shown in the bottom right-hand panel. CRs and different detector artifacts, such as hot and bad pixels are visible in all images.

exposures, then the third image will allow us to identify the outlier measurement and discard the affected exposure.

The other 14 WDs were observed only in Cycle 22, by collecting five to seven dithered exposures for each filter. The *HST* primary CALSPEC standards were observed in Cycle 22 with six to eight exposures per visit, for a total of three visits (18 to 24 exposures) in all filters, spanning an average time interval of about 1 yr and 3 months, from 2014 September/November to 2015 November/2016 January. For more details on the observation strategy, please see the log in Table 4.

Parallel observations with the Advanced Camera for Surveys in the F475W and F775W filters were collected, including stars a few arcminutes away from the candidate spectrophotometric standards. The analysis of these images and an evaluation of the usefulness of the observed stars as supplementary standard stars will be presented in a forthcoming paper.

3.1. Image Processing

WFC3 UVIS images for Cycle 20 and Cycle 22 were processed with version 3.3 of the WFC3 calibration pipeline (cal_wf3) that treats the two chips—UVIS1 and UVIS2—individually (Deustua et al. 2017). The image photometry reference table (IMPHTTAB) that we used is z7n21066i_imp. fits and it writes PHOTFLAM values for a 10 pixel aperture (Deustua et al. 2016). A newer IMPHTTAB file was released in June 2017, which provides PHOTFLAM values for an infinite aperture, although it was not used to reduce our dataset. Cycle 20 images were collected by using the full UVIS1 aperture (UVIS1-FIX), with the target star placed in its center. Few pixel dithered exposures were collected to correct for detector

artifacts and CRs (see the observation log in Table 4). The subarray UVIS2-C512C-SUB aperture was used for Cycle 22 observations, with the target star placed in its center and the exposures dithered by a few pixels (less than $\sim\!20$). This allowed us to place the WDs closer to the read-out amplifier to mitigate the charge transfer inefficiency effects.

Starting from version 3.3, the WFC3 calibration pipeline scales UVIS2 fluxes to the UVIS1 chip by default. Therefore, we manually re-processed all the images with *cal_wf3* by setting FLUXCORR = OMIT in the header to avoid the flux scaling and to keep the photometry on the UVIS2 detector system. Later on, the scale factor between Cycle 20 UVIS1 and Cycle 22 UVIS2 photometry will be estimated and applied to the measured magnitudes (see Section 4.4).

All of the WFC3-UVIS images were corrected for Charge Transfer Efficiency (CTE) by using the official WFC3 software ¹¹ and the WFC3 Pixel Area Map (PAM) was applied ¹² to correct for differences in the area of each pixel in the sky due to the geometric distortion of WFC3-UVIS.

WFC3 infrared (WFC3-IR) images were collected by using the full camera aperture (IR-FIX) and placing the targets at the center of the detector with every exposure dithered by 10–20 pixels. This strategy was used to avoid self-persistence. For the three primary WDs, observations were collected by using the IRSUB256-FIX and the IRSUB512-FIX subapertures to allow more exposures in the same orbit. Images were processed with the *cal_wf3* calibration pipeline and the WFC3 PAM was applied.

¹¹ http://www.stsci.edu/hst/wfc3/ins_performance/CTE

¹² http://www.stsci.edu/hst/wfc3/pam/pixel_area_maps

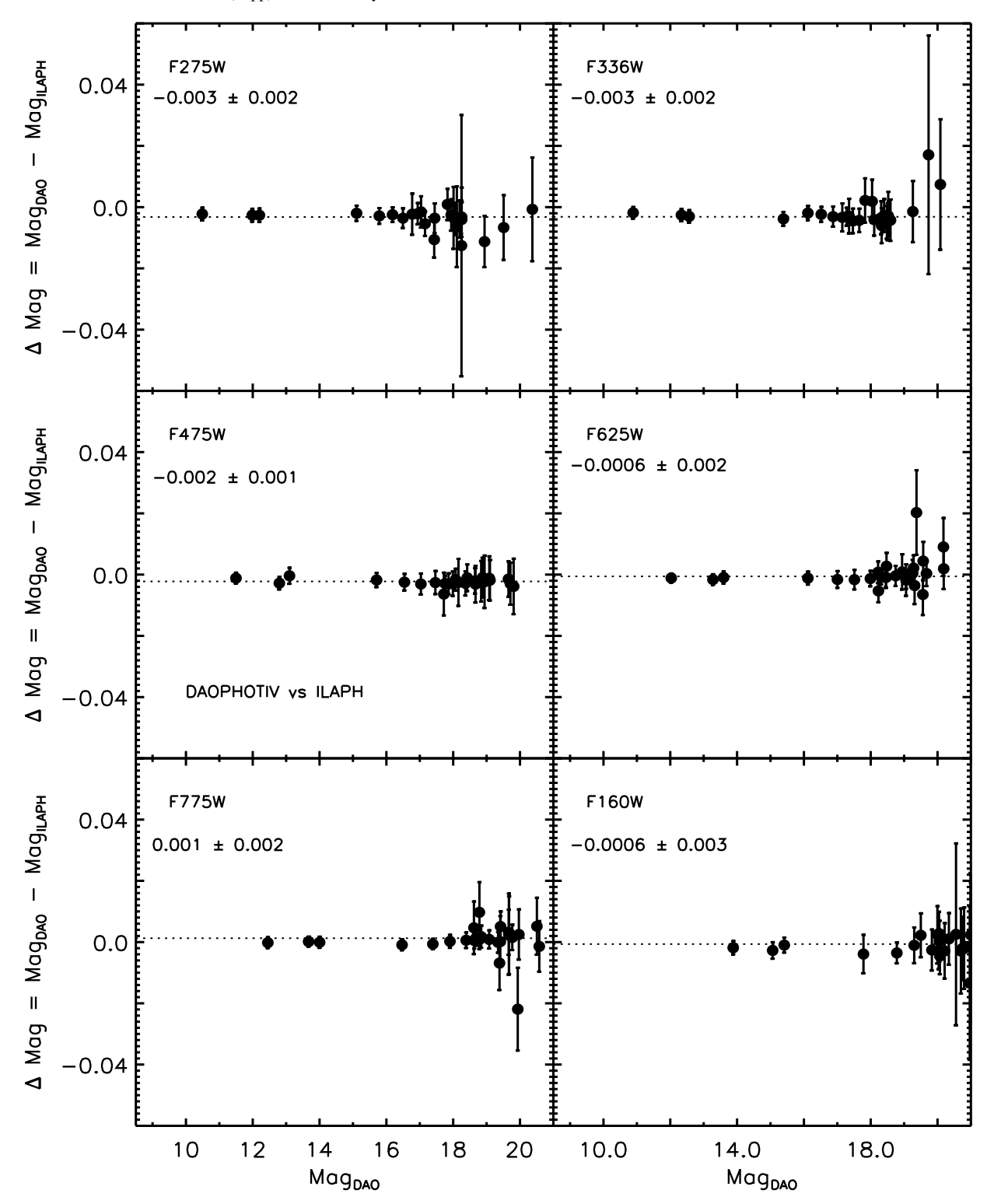


Figure 5. Comparison of DAOPHOT and ILAPH aperture photometry magnitudes, Δ Mag = Mag_{DAOPHOT} - Mag_{ILAPH}, in six filters as a function of DAOPHOT magnitude, for the 23 candidate spectrophotometric DAWDs and the 3 *HST* primary CALSPEC standards. The mean magnitude differences with the relative dispersions are shown.

4. Optimal Extraction of the White Dwarf Photometry

Following a series of tests, we have discovered that the individual WFC3 images cannot be combined in the standard pipeline reduction and be expected to yield measurements with milli-mag level uncertainties. In particular, the anti-coincidence method of eliminating CR events can affect the cores of stars.

In reducing Cycle 20 WFC3 data, NA16 found that combining images with the drizzle algorithms (Drizzle Pac¹³) by using the pipeline default input parameters is not suitable for our purpose. Although drizzling eliminates CRs, it also introduces

¹³ http://drizzlepac.stsci.edu/

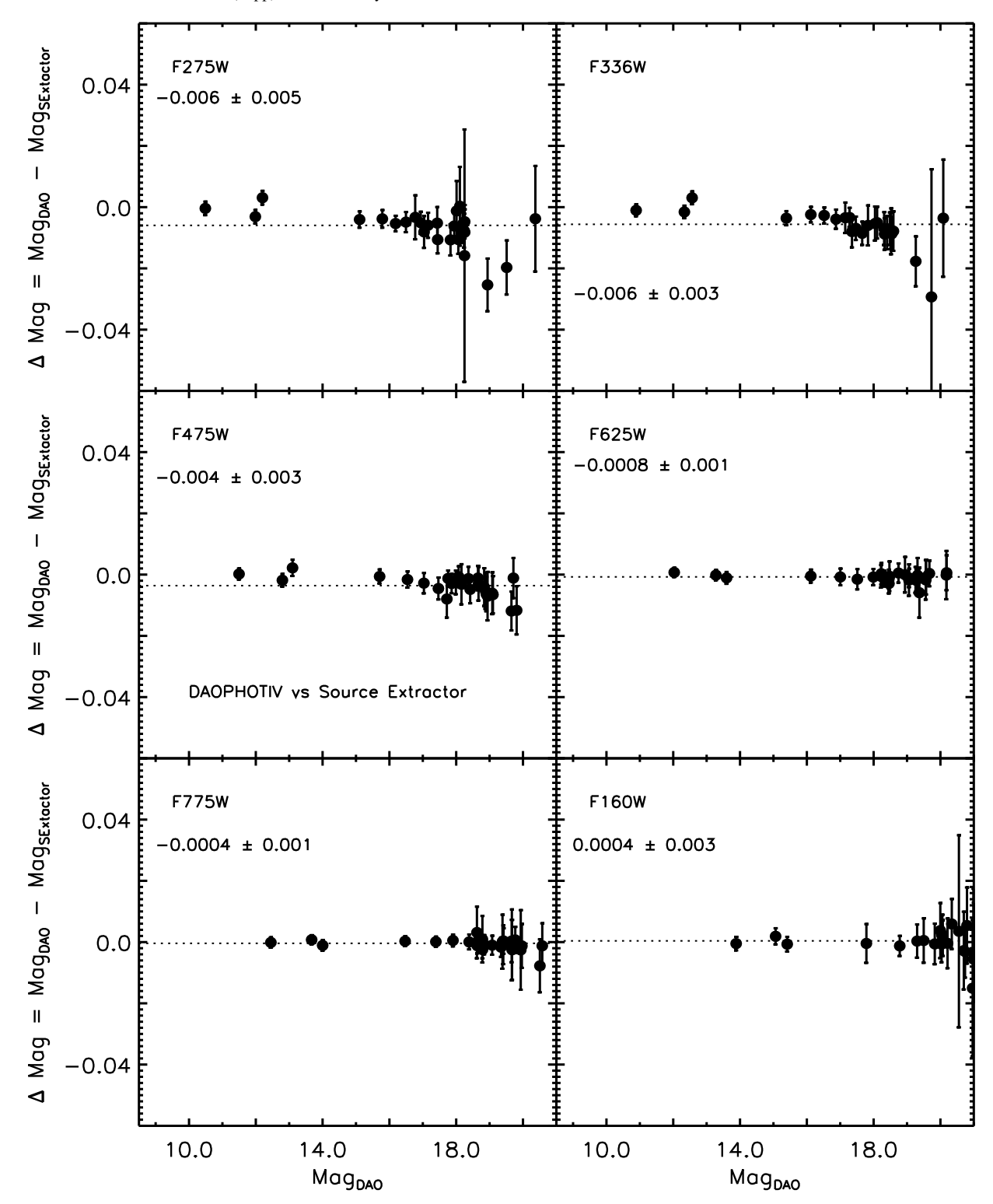


Figure 6. Same as Figure 5 but for DAOPHOT and SExtractor magnitudes, Δ Mag = Mag_{DAOPHOT} - Mag_{SExtractor}

noise by over-correcting for differences in the cores of bright stars. Therefore, to avoid compromising the quality of the good images, where the target star is unaffected by a CR in its measuring aperture, we had to manually discard any image with a CR event over the measurement aperture on those few occasions it happened (3%–4% of the total number of images).

Our current reduction strategy involved performing photometry on the individual CTE-corrected images (FLC) for the

WFC3-UVIS detector, and on the FLT images for WFC3-IR, after having applied the PAM correction. We had to check all of the $\sim\!\!800$ images for the presence of a CR event inside the star aperture radius. This was a rather tedious procedure but it allowed us to obtain a sub-percent accurate photometry for our set of standard stars.

We used three completely independent packages to perform aperture photometry on all of the images: (1) Source Extractor

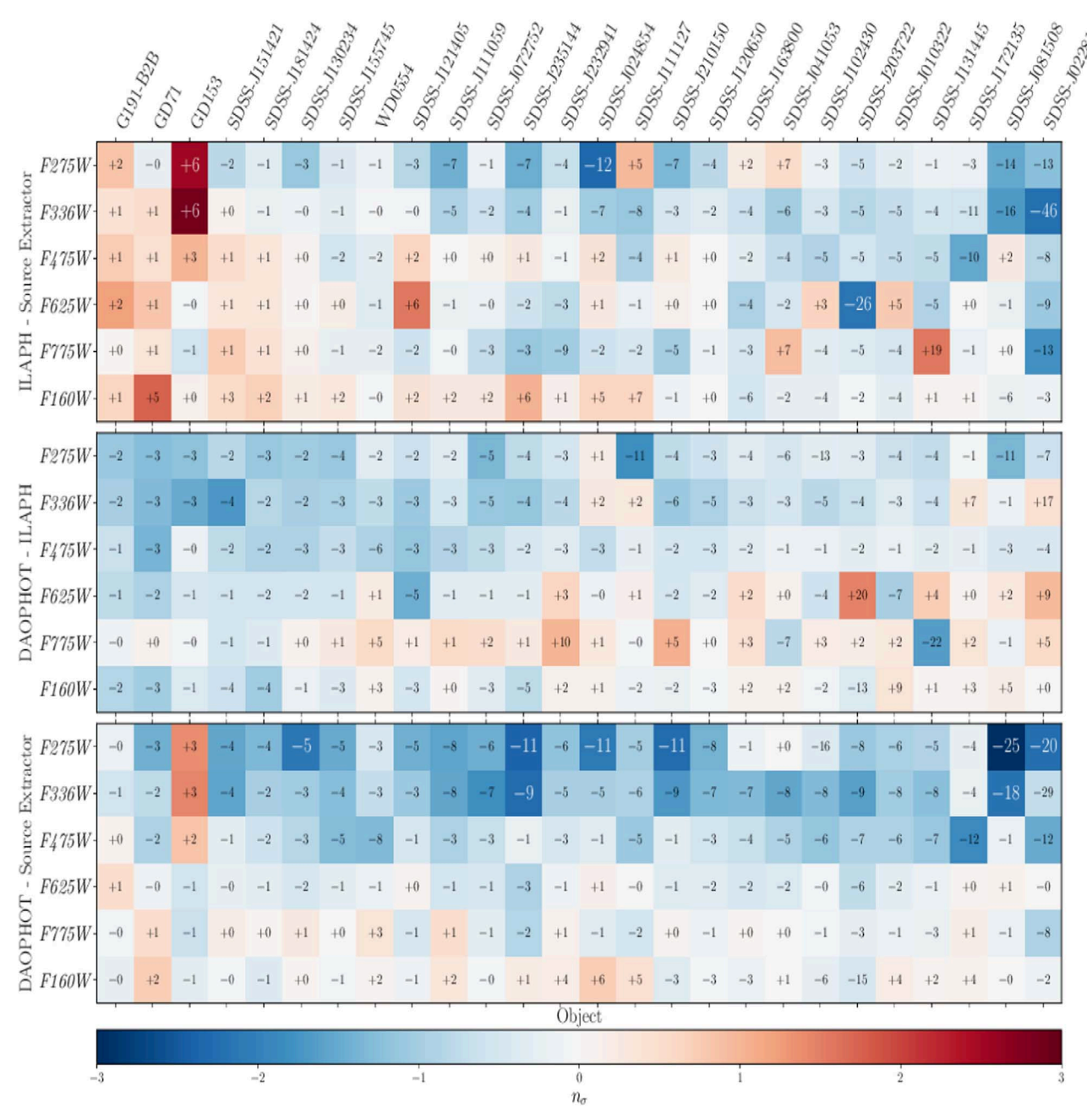


Figure 7. Comparison matrix between magnitudes measured with ILAPH, DAOPHOT, and Source Extractor for the 23 candidate standard DAWDs and the 3 *HST* primary CALSPEC stars in all the WFC3 observed filters. The color scale is labeled at the bottom of each panel and the name of the stars is marked at the top of the panels. Stars are sorted by *g*-band magnitude, starting with the brightest on the left. Filters are labeled on the left-hand side of each panel. The color of the box is bluer when the weighted magnitude difference between the two methods is negative (i.e., when the magnitude of the first labeled method is brighter compared to the magnitude of the second method), while it is red when the weighted magnitude difference is positive. See text for more details.

(Bertin & Arnouts 1996, hereafter SExtractor); (2) DAOPHO-TIV (Stetson 1987, hereafter DAOPHOT); and (3) ILAPH (an IDL based interactive program for aperture photometry and growth curve analysis written by A. Saha, customized for the data at hand).

Performing photometry by using different packages may generate systematic differences in the results. Our strategy will then enable us to track down possible systematic issues due to the data reduction method that we used. Moreover, it will allow us to determine realistic uncertainties, which is of paramount importance for our study because analysis downstream depends on these for weights.

After analyzing photometric growth curves for a sample of faint and bright WDs, we found the optimal aperture radius for the photometry to be 7.5 pixels for the WFC3-UVIS images and 5 pixels for the WFC3-IR images, i.e., $\sim\!0.^{\!\prime\prime}\!3$ and $\sim\!0.^{\!\prime\prime}\!65$, respectively. The local sky background for each source was estimated in a rectangular region (SExtractor) and a circular (DAOPHOT, ILAPH) annulus around the aperture centered on the star. In the case of SExtractor, the box has a size of 20 pixels and the sky background in this region is estimated as a modified mode (2.5 \times Median–1.5 \times Mean) after an iterative sigma-clipping rejection of the outlier pixels. DAOPHOT uses the mode (3.0 \times Median–2.0 \times Mean) as the best sky

estimator after an iterative sigma-clipping rejection of the outliers. However, in non-crowded stellar fields, if the mean sky value in the selected annulus is smaller than the median, then the mean of the sky value is used as best sky estimate. In this case, we used an annulus with radii $r_{\rm in}=156$ and $r_{\rm out}=165$ pixels around the target DAWDs. We selected these values since 156 pixels corresponds to $\sim 6''$ and it can be considered to infinity relative to the star's position.

ILAPH was configured to use the median sky value in the selected annulus around the stars as the best sky estimator. This is more robust than the mean because the latter is vulnerable to the presence of contaminating objects in the annular sky aperture. For UVIS, an aperture radius of 7.5 pixels and an annulus with radii $r_{in} = 20$ and $r_{out} = 30$ pixels was used for the sky. While this measurement procedure disregards light outside the respective apertures due to the extended skirt of the stellar point-spread function (PSF), it is asserted that the skirt affects all stars equally. In addition, as long as we measure the bright HST primary CALSPEC standards in exactly the same way as our target DAWDs, we are measuring instrumental magnitudes that all share a common ZP offset. For the IR images (F160W), ILAPH was used in the same way but with an aperture radius of 5 pixels and a sky aperture annulus from 14 to 21 pixels. The sky apertures were chosen with some experimentation: stability in the measured instrumental magnitude values from image to image for the same object was used as the criterion for selection. The program also looks at the pixel to pixel scatter within the annular sky aperture and it propagates that variance into the measurement error estimate. ILAPH was customized to use the actual fluctuation in the sky background and not just from the shot noise (Poisson statistics) of the adopted sky brightness in the calculation of photometric uncertainty. Subsequent analysis utilizes the uncertainties as weights, which makes it crucial to get this estimate to be as realistic as possible.

An accurate estimate of the sky background is fundamental for our analysis. In particular, a wrong estimate of the sky background has a greater effect on the faintest DAWDs and can introduce a systematic bias in the measurements. Figure 5 shows the comparison between the measurements in the six filters—F275W, F336W, F475W, F625W, F775W, and F160W—obtained with DAOPHOT and ILAPH (Δ Mag = Mag_{DAOPHOT} – Mag_{ILAPH}) for all the observed DAWDs as a function of the measured DAOPHOT magnitude. The single epoch magnitudes, corrected for the instrumental effects, including the sensitivity difference between Cycle 20 and Cycle 22, were averaged as described in Section 7.

The plot shows that measured aperture magnitudes with DAOPHOT and ILAPH are, within uncertainties, in very good agreement: with a biweight mean difference less than 0.003 mag in all filters, and with a dispersion less than 0.003 mag for all UVIS filters and less than ~0.003 mag for F160W. A couple of stars—SDSSJ102430.93–003207.0 and SDSSJ172135.97+294016.0—show very large uncertainties, ~0.02 and 0.04 mag, respectively, in the F275W and the F336W filters. The first DAWD was already problematic in NA16 Cycle 20 measurements, and is a candidate variable (see Section 7.1). Star SDSSJ172135.97+294016.0. has no clear problems on the images, but an undetected faint CR falling on the aperture radius could be the culprit. However, this star is already excluded from our set of spectrophotometric standards

due to its low effective temperature ($T_{\rm eff} \sim 9000$ K), so we will not investigate this issue further.

The same comparison is performed for all the measurements obtained with DAOPHOT and SExtractor in Figure 6, where $\Delta \text{Mag} = \text{Mag}_{\text{DAOPHOT}} - \text{Mag}_{\text{SExtractor}}.$ In this case, the measurements agree quite well within uncertainties but, on average, they have a larger dispersion, up to 0.005 mag for F275W. Moreover, a slight trend with magnitude is present, with SExtractor magnitudes being fainter at fainter magnitudes.

To further investigate this issue, we produced a matrix comparison of the three data reduction methods in Figure 7. Each depicted box is color-scaled according to the weighted magnitude difference between two of the three methods, estimated as:

$$\Delta Mag = (Mag_{meth1} - Mag_{meth2}) / \sqrt{err_{meth1}^2 + err_{meth2}^2}$$
 (1)

where Mag_{methX} and err_{methX} are the magnitudes and magnitude errors for each method, respectively.

Each box corresponds to a star measured in one of the six filters, sorted by magnitude (brightest on the left of the matrix), and the numeric text value is the magnitude difference, in millimag, between the measurements of the two methods. The color of the box is bluer when the weighted magnitude difference between the two methods is negative (i.e., when the magnitude of the first labeled method is brighter compared to the magnitude of the second method), while it is red when the weighted magnitude difference is positive. The text in the boxes is larger and white when the difference in magnitude between the two methods is larger than 2σ ; i.e., significant compared to photometric errors.

The middle panel of the figure confirms that ILAPH and DAOPHOT provide very comparable results within the uncertainties, with no significant magnitude difference for all the measured stars in all filters. However, for fainter stars (right-hand section of the matrix), a very slight trend with color is present, in the sense that these stars are fainter in the redder filters (F625W, F775W, and F160W) when measured with DAOPHOT (redder boxes on the bottom right of the panel). However, this trend is well within the uncertainties of the measurements.

The top and the bottom panels of Figure 7 confirm that SExtractor magnitudes are systematically fainter compared to ILAPH and DAOPHOT magnitudes in all filters, as suggested by Figure 6 (bluer boxes in the panels). This difference has either a magnitude and a color effect: (1) magnitudes for brighter stars seems to agree between SExtractor and the other two methods, or to be brighter when measured with SExtractor (left part of the panels), while fainter stars are fainter when measured with SExtractor (right part); (2) the discrepancy is larger for the bluer filters (F275W and F336W, top part).

To understand this discrepancy, we compared the sky background values estimated with the three different methods. SExtractor local sky background shows systematically higher values when compared to DAOPHOT and ILAPH sky values. This difference in sky values is larger at fainter magnitudes, making SExtractor magnitudes fainter for fainter stars. However, the DAOPHOT and ILAPH sky values agree quite well within the uncertainties.

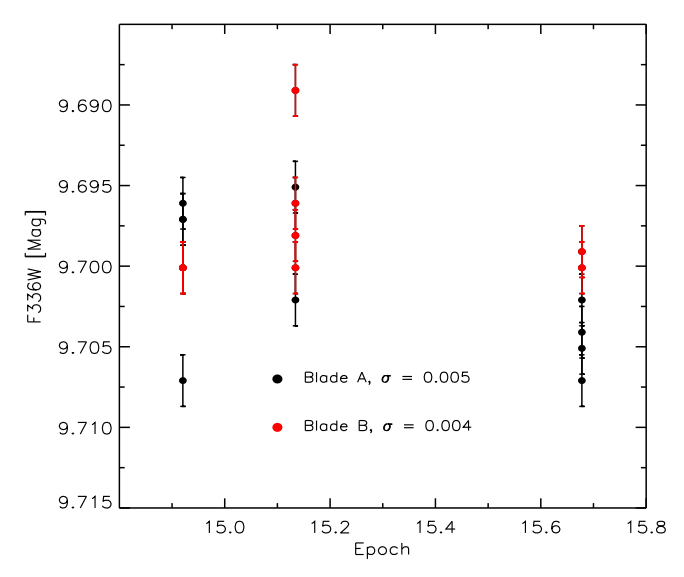


Figure 8. Aperture magnitudes in the F336W filter for star G191B2B measured with shutter blade A (black points) and B (red) plotted vs. the epoch. The error bars are labeled. The standard deviation of the measurements for the two blades is also shown.

4.1. IR Photometry

The WFC3-IR detector is affected by persistence; i.e., the residual signal of a large incident light level that can last on the images from minutes to days (Long et al. 2011, 2013; Gennaro et al. 2018). Some of our observations could have been scheduled after IR observations that cause persistence or bright objects in the images could have caused persistence in the same exposures. To verify this, we checked all of the images for the level of external (due to previous observations) or internal (due to objects in the same exposure) persistence by using the available WFC3 persistence tool. 14 This search revealed that none of our observations was heavily affected by external or internal persistence, with the fraction of pixels with a residual signal larger than 0.01 e⁻ s⁻¹ being less than 0.1%. Note that the dark current signal for WFC3-IR is 0.04 e⁻ s⁻¹. Three visits -one for star G191B2B, one for GD153 and one for SDSSJ181424.075+785403.048—have a fraction of pixels with a residual signal larger than 0.01 e⁻ s⁻¹ of 0.16%, 0.25% and 0.33%, respectively, due to external persistence. However, the affected pixels do not overlap with the target DAWDs location, being more than 50 pixels away. Internal persistence is not an issue for all our observations. Brighter stars, such as the three primary WDs, could cause self-persistence on the IR images. To avoid this, we dithered each exposure by more than 10 pixels, as recommended by the WFC3 team.

Another issue affecting IR observations is the count-rate nonlinearity (CRNL); i.e., the nonlinearity of the detected counts with the total incident flux on the camera. This effect may be relevant for our observations because the target DAWDs cover a range of more than 10 mag. The CRNL was characterized for the WFC3-IR camera by Riess (2010, 2011), Riess & Petro (2010) and who measured 0.010 \pm 0.0025 mag per dex for the F160W filter. The net effect of CRNL is that photometry of very faint stars—i.e., background dominated—appears fainter (Riess & Petro 2010). An accurate characterization of the CRNL for the program IR photometry, based on the observations and on models, will be provided in NA19.

Therefore, we do not apply any CRNL corrections on the photometry presented in this paper.

4.2. Shutter Shading

The accuracy of the measured magnitudes on WFC3-UVIS could be affected by the shutter shading effect. For the brightest stars in our sample, we used very short exposures times (t < 2 s). For these short times, shutter vibration can affect the actual duration of the exposures, leading to fainter measured magnitudes on the image. This effect was studied in detail by the WFC3 team and discussed in different Instrument Science Reports (Hilbert 2009; Sabbi 2009; Sahu et al. 2014, 2015). Shutter vibrations in short exposures also results in a broadening of the observed PSF. When observing using shutter blade B, the Full-Width-Half-Maximum of the stellar images is systematically larger than when using blade A. The larger shutter vibrations when using blade B can introduce a flux measurement uncertainty up to $\sim 2\%$ for photometry performed with aperture radii smaller than 5 pixels (Sabbi 2009).

For our WFC3-UVIS data, we used an aperture radius of 7.5 pixels and so shutter shading should not affect images collected by using blade B. However, we checked for the presence of this effect on the images of the brightest of the primary CALSPEC standards—G191B2B. The selected F336W images were collected in a sequence of 1.0 s exposures alternating the two shutter blades (ABAB...). Figure 8 shows instrumental aperture magnitudes in the F336W filter for G191B2B measured with shutter blade A (black points) and B (red) plotted versus the observing epoch. The standard deviation of the measurements is 0.005 and 0.004 mag for blade A and B, respectively. The plot shows that there is not significant difference between magnitudes measured on images collected by using blade A or B. We performed the same experiment for G191B2B images collected with the other UVIS filters and obtained similar results.

The exposures times for the other DAWDs are longer than for G191B2B (see the observing log in Table 4), so we did not verify for shutter blade effects in all the other observations and we can safely assume that none of the exposures is affected.

4.3. Testing Photometry for Crowding Effects

Another factor that could affect the accuracy of measured magnitudes is the presence of unseen neighbor stars in the DAWD aperture radius. To test this hypothesis, we performed some artificial star (AS) tests simulating stars of different brightness with centroids from 0 to 5 pixels away from the DAWD. We simulated stars from 3 to 7 mag fainter than the DAWDs. The results of these simulations show that AS more than 6 mag fainter than the target DAWD falling in the 7.5 pixel aperture radius do not affect the measured magnitudes. Meanwhile, brighter neighbor stars falling inside the aperture radius could affect the photometry of the target DAWD by adding $\sim 1\%$ of noise to the measurement.

However, our candidate standard DAWDs are in sparsely populated stellar fields and the observed WFC3 sub-array field of view (FoV) is \sim 20". We checked the PS catalog to look for the presence of other stars in the observed FoV and found only the target DAWDs or a maximum of other two objects (well outside the aperture radius) down to the PS detection limit ($g \sim 23$ mag), so more than 5 mag fainter than our targets. We

¹⁴ https://archive.stsci.edu/prepds/persist/search.php

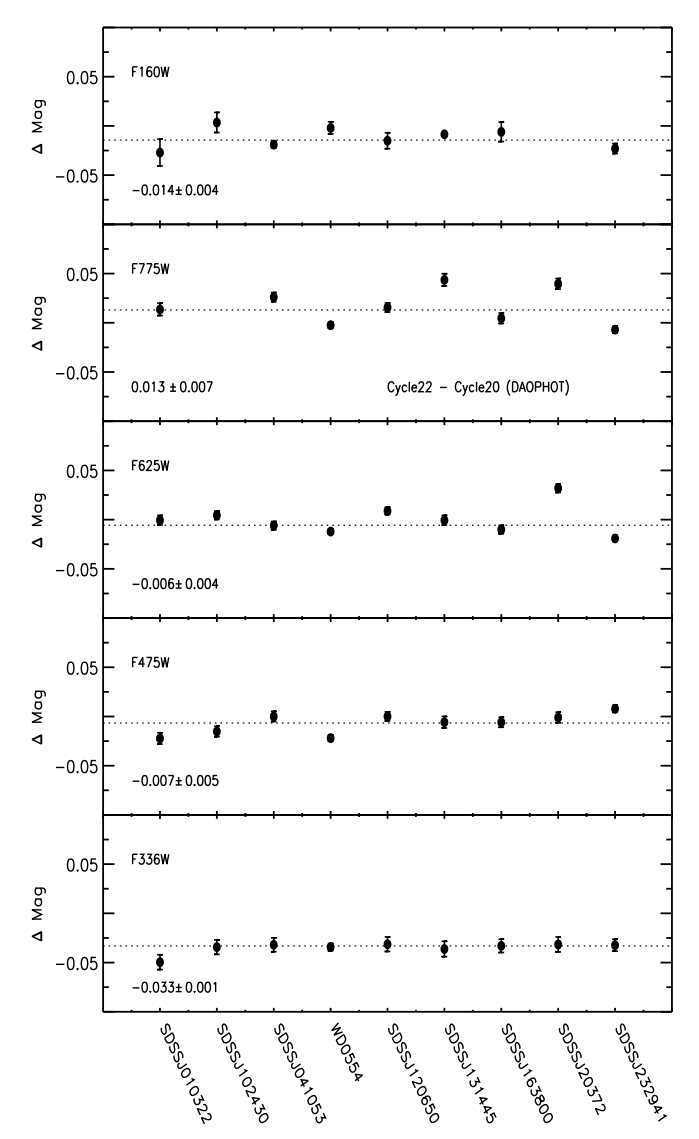


Figure 9. Comparison of Cycle 20 and Cycle 22 average magnitudes measured with DAOPHOT in six filters, namely F275W, F336W, F475W, F625, F775W, and F160W for nine *equatorial* WDs. The weighted mean magnitude differences between the two observing cycles with the relative errors are also labeled.

can then safely assume that the photometry of the DAWDs is not affected by contamination of unseen neighbor stars.

4.4. Magnitude Offset between the HST Observing Cycles

Images in the five filters—F336W, F475W, F625W, F775W, and F160W—were collected in Cycle 20 and Cycle 22 for the nine *equatorial* WDs. For this subset of targets, we then have two sets of measurements. Because the primary CALSPEC WDs, which anchor our photometry to the *HST* system, were only observed in Cycle 22, we need to estimate the magnitude offset between the two cycles and calibrate Cycle 20 measurements to Cycle 22. Cycle 20 observations were performed by using the full UVIS1 aperture, while Cycle 22 exposures were collected with a UVIS2 sub-array. The magnitude offset needs to take into account the difference due to observing with two different WFC3 detectors and all the effects due to observations taken more than 2 yr apart.

Figure 9 shows the comparison between Cycle 20 and Cycle 22 magnitudes in the five filters for the nine *equatorial* WDs. Star SDSSJ102430.93–003207.0 has very discrepant measurements in the F775W filter (Δ Mag \sim -0.21); NA16 claim that this WD might be variable. The same applies to star SDSSJ203722.169–051302.964, where the F160W measurements are in strong disagreement between the two observing cycles (Δ Mag \sim 0.27). The spectrum of this WD shows emission features in the core of the Balmer absorption lines, which indicates the presence of a low-mass companion star (see Section 6 for more details). Therefore, both stars were removed from the sample to estimate the magnitude offset.

The offsets are between ~ 0.005 and ~ 0.03 mag, depending on the filter, with an average dispersion of 0.005 mag. Columns 8 and 9 of Table 6 list the magnitude offsets and their uncertainties between the two HST observing cycles in the different filters.

After having applied these magnitude offsets, we estimated the weighted mean instrumental magnitudes for all the 23 observed DAWDs based on the photometry of the two cycles.

5. Photometric Stability of the Candidate Standard DAWDs

To assess the 23 candidates as stable standards, we monitored them by collecting time-series data with the Las Cumbres Observatory (LCO) network of telescopes (proposals LCO2016B-007, LCO2017AB-002, PI: Matheson).

WDs can vary for several reasons, depending on their effective temperature, atmosphere abundance and presence of magnetic activity or of an unseen faint companion star.

Hydrogen-rich atmosphere WDs might present gravity-mode pulsations around $T_{\rm eff} \sim 12,000 \, {\rm K}$ (Fontaine & Brassard 2008, ZZ Ceti pulsators). Our DAWDs were selected to have temperatures ($T_{\rm eff} \gtrsim 20,000 \, {\rm K}$) outside the ZZ Ceti instability strip, so we do not expect them to be pulsators (note that SDSS-J172135.97+294016.0 will be removed from the network of standards since it has $T_{\rm eff} = 9261 \, \rm K$). Strong magnetic fields can also cause flux variations in WDs with a timescale from hours to days. These variations can be due to magnetically confined spots of higher opacity modulating the stellar flux via stellar rotation (Dupuis et al. 2000; Holberg & Howell 2011). Alternately, magnetic variations can be due to to spots in the convective atmosphere (Brinkworth et al. 2004, 2013). However, the 23 candidate standard DAWDs have effective temperatures above \sim 20,000 K, and their atmosphere are fully radiative, so they should not vary due to the presence of spots. Moreover, their spectra did not show Zeeman splitting of the Balmer lines indicative of the presence of a strong magnetic field (see Section 6). However, the selected DAWDs could still vary due to the presence of an unseen faint companion star, or to unknown factors, and we need to characterize the amount of flux variation, if present, before setting these stars as spectrophotometric standards. A recent study by Hermes et al. (2017), based on precise Kepler time-series photometry, showed that \sim 97% of apparently isolated WDs are stable or show less than 1% flux variations and can still be used as spectrophotometric standards. Hermes et al.'s sample included mostly DAWDs and also included several helium- or carbon-dominated atmosphere WDs, with temperatures hotter than $\sim 8000 \text{ K}$.

On the basis of the criteria used to select the 23 DAWDs and previous studies, we do not expect a large fraction of our candidate spectrophotometric standards to vary. However,

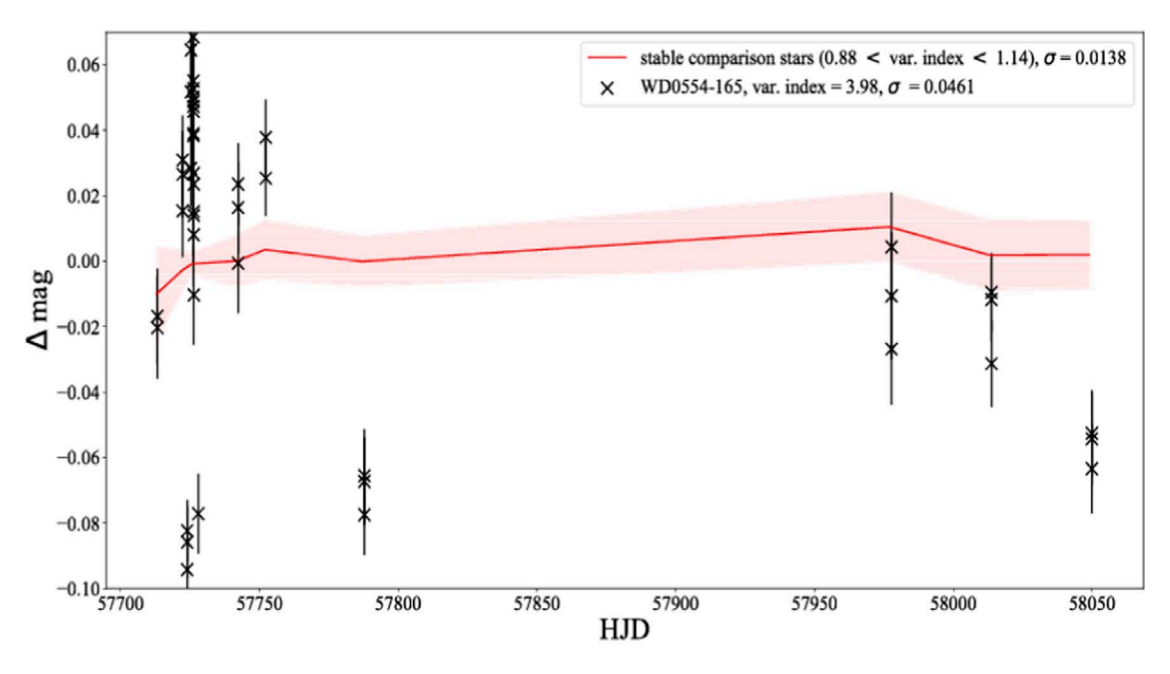


Figure 10. Single epoch minus the mean instrumental magnitude measurements for WD0554–165 as a function of observing epoch (black crosses). Averaged and binned relative magnitudes for a set of stable stars of comparable instrumental magnitude in the same field of view are overplotted as a red shaded area. The variability index of the selected stars and the measurement dispersions are listed. Error bars are shown.

these 23 DAWDs have not yet been subject to a consistent and well-defined observational campaign to demonstrate a lack of variability at a wide range of timescales. WFC3 observations are obtained within a short time frame for each target, which makes them unsuitable as tests of variation. In addition, prior ground-based surveys (SDSS, PanSTARRS) do not have the necessary temporal coverage and *GAIA* does not yet provide variability constraints on these stars.

5.1. Time-series Photometry

LCO observations consist of a sequence of geometrically spaced exposures in the Sloan *g* filter, ranging from minutes to month-long timescales. A minimum of 20 exposures for each target were collected, spread over 2–3 months at different time intervals, for a total of about 800 images.

PSF photometry was performed with DAOPHOTIV/ALL-STAR (Stetson 1987) and ALLFRAME (Stetson 1994). The average FWHM for each frame was measured by using Source Extractor to exclude observations affected by poor observing conditions or bad focus, and these handful of images were excluded from the analysis. All the exposures for each target were flux scaled to the best image, defined by the frame with the smallest average FWHM, which was used as a reference image. Light curves were then produced for each of the 23 targets.

To select candidate variables we used the Welch & Stetson (1993) variability index W:

$$W = \sqrt{\frac{1}{n(n-1)}} \sum_{i=1}^{n} \frac{m_i - \bar{m}}{\sigma_i}$$
 (2)

where m_i are the individual measurements and \bar{m} is the mean weighted magnitude of each identified object, and n is the total number of frames. The Welch–Stetson variability index was calculated for all of the stars (from ~ 500 to 1000) in the FoV. A sample of *stable* comparison stars was selected for each of

the 23 DAWD observation. This group of *stable* stars has a detection in every frame and a variability index, *var index*, ≤ 1.2 , the sharpness of the PSF in the range -0.5 < sharpness < 0.5, to exclude extended objects and CRs, and a proximity in magnitude to the target WD within ~ 0.2 mag.

An absolute calibration of the photometry is not performed because our goal is to demonstrate the lack of variability of the candidate standard DAWDs. However, we need to take into account spurious flux variations due to instrumental and atmospheric effects (observations are performed with different telescopes and detectors and from different sites in different conditions). The light curves of the selected *stable* stars are then compared to the light curves of the WDs in the same field. The variation around the mean of the *stable* star magnitudes was averaged and the average 1σ dispersion was estimated. This dispersion is used as a variability threshold for the systematic observational and instrumental effects.

Figure 10 shows the single epoch minus the weighted mean instrumental magnitude as a function of the Heliocentric Julian Date (HJD) for WD0554–165 (black crosses). The averaged and binned relative magnitudes for a set of *stable* stars of comparable instrumental magnitude in the same FoV are also plotted as a red shaded area. The selected comparison stars have a variability index less than 1.2 while the WD0554–165 has a variability index of 3.98. WD0554–165 shows clear signs of variability, with variations of almost 0.2 mag and a measurement 1σ dispersion of \sim 0.05 mag, compared to the *stable* star dispersion of σ 0.01 mag. Figure 11 shows the same plot but for a stable DAWD, SDSSJ235144.29 +375542.6, whose variability index is \sim 1 and the dispersion of the measurement is \sim 0.015 mag, which is smaller than the measurement dispersions for the *stable* stars, σ 0.018 mag.

The light curve for SDSSJ20372.169–051302.964, which is a candidate binary system from spectroscopic data, shows variability with a dispersion of the measurements of $\sigma \sim 0.04\,\mathrm{mag}$, which is a factor of 4 larger than the comparison star

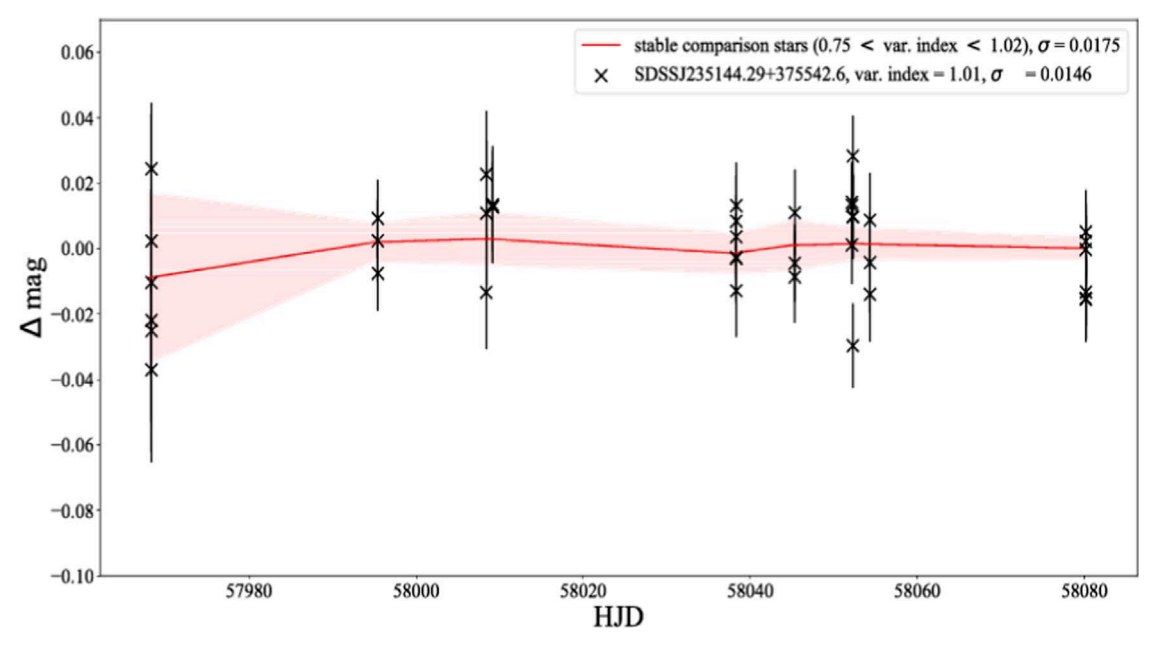


Figure 11. Same as Figure 10 but for star SDSSJ235144.29+375542.6.

measurement dispersion, $\sigma \sim 0.01\,\mathrm{mag}$, thus confirming its binary nature.

Although the other two stars in the sample—SDSSJ010322.10–002047.7 and SDSSJ102430.93–003207.0—show hints of variability, more and deeper exposures are needed to confirm these preliminary results.

Stars SDSSJ20372.169–051302.964 and WD0554–165 will be excluded from our network of spectrophotometric standard DAWDs due to their variable nature.

A more detailed analysis of the LCO photometry and the DAWD light curves will be presented in a forthcoming paper. We also plan to follow-up the candidate variable DAWDs with more observations from a larger ground-based telescope to understand the origin of their variability.

6. Spectroscopic Observations

The spectra of the DAWDs are used to determine $T_{\rm eff}$ and $\log g$. These values are derived from the shape of the H I Balmer line profiles from ${\rm H}\beta$ to ${\rm H}\zeta$. We flux-calibrated the spectra to facilitate the analysis of the Balmer lines but the overall shape of the spectrum will retain uncertainties introduced by the flux calibration process and by the inherent uncertainty in the standard stars used. We emphasize that the spectral shapes are not critical to the ultimate analysis of these DAWDs as spectrophotometric standards. The deviation of the calibrated spectral shape from a model spectrum is treated as a nuisance parameter in the fitting process, thus minimizing the calibration error improves the uncertainties in the end result. Nonetheless, the values of $T_{\rm eff}$ and $\log g$ from the Balmer lines in concert with the photometry provide the ultimate calibration of these stars.

We used two different facilities to obtain spectra of our standard star candidates. As part of the *HST* photometry proposal, we were awarded Gemini time. This amounted to 43 hr from Cycle 20 (split over Gemini semesters 2013A and 2013B) and 28.1 hr from Cycle 22 (split over Gemini semesters 2015A and 2015B). For most of this time, we used Gemini South, but we

also used Gemini North for the northern targets. At each site, we used the Gemini Multi-Object Spectrograph (GMOS, Hook et al. 2004) in queue mode with a long slit to obtain the spectra. For the 2013A and 2013B semesters, we used the 1".5 slit; while for 2015A and 2015B, we used the 1".0 slit. The three GMOS detectors are not contiguous, so we used two different grating tilts to fill in the inter-chip gaps. The final spectra are continuous from 3500 to 6360 Å with a dispersion of 0.92 Å/pixel. The resolution of the spectra is a function of the seeing at the time of observation given the relatively wide slit and the generally good seeing conditions at the Gemini sites. Determining the resolution is an element of the data analysis process that will be described in a later paper.

We found that the Gemini data were generally not of sufficiently high quality for our purpose. The throughput of the GMOS system in the blue is poor. In addition, standard stars and other calibrations were frequently not obtained in conjunction with the spectra of the white dwarfs. Finally, despite our request, the observations were typically not obtained at the parallactic angle (Filippenko 1982) so slit losses resulting from atmospheric dispersion resulted in compromised shapes for the SEDs of the stars. Because of these issues, we instituted a program at the MMT Observatory to obtain alternate spectra of our DAWDs.

At the MMT, we used the Blue Channel spectrograph (Schmidt et al. 1989) with the 300 line mm⁻¹ grating. We had a total of four successful observing nights spread over three epochs. For most of the observations, we used the 1."0 slit, but we used the 1."25 slit for one epoch. The wavelength coverage runs from 3400 to 8400 Å with a dispersion of 1.95 Å/pixel. All observations were obtained at the parallactic angle and standard stars were observed on the same night. As with the GMOS data, the resolution of the spectra depends on the seeing at the time of observation.

Details of the observations with both facilities are presented in Table 5. We used standard IRAF¹⁵ routines to process the

¹⁵ IRAF is distributed by the National Optical Astronomy Observatory, which is operated by AURA under cooperative agreement with the NSF.

Table 5
Log of the Spectroscopic Observations

Star	UT Date	Tel. ^a	Range (Å)	Res. ^b (Å)	P.A. ^c (°)	Airmass	Flux Std.d	Slit (")	Exposure (s)
G191B2B	2015 Jan 24	MMTO	3400-8400	8	-111.8	1.2	Feige34	1.0	8
GD153	2015 May 18	MMTO	3400–8400	8	-52.9	1.0	BD+284211	1.0	15
GD71	2015 Jan 24	MMTO	3400–8400	8	12.8	1.0	Feige34	1.0	10
SDSSJ010322.19-002047.7	2013 Nov 29	GEMINI-S	3500–6360	10	180.0	1.2	GD71	1.5	6 × 1500
SDSSJ010322.19-002047.7	2015 Oct 11	MMTO	3400–8400	8	13.5	1.2	BD+284211	1.25	2×1200
SDSSJ022817.16-082716.4	2013 Oct 23 ^e	GEMINI-S	3500–6360	10	0.0	1.2	GD71	1.5	7×1500
SDSSJ024854.96+334548.3	2015 Oct 08 ^e	GEMINI-N	3520–6360	7	232.0	1.1	BD+284211/G191B2B	1.0	8 × 999
SDSSJ024854.96+334548.3	2015 Oct 11.5	MMTO	3400-8400	8	92.4	1.1	BD+284211	1.25	5×1200
SDSSJ041053.632-063027.580	2013 Dec 04 ^e	GEMINI-S	3500–6360	10	180.0	1.2	GD71	1.5	6×1500
SDSSJ041053.632-063027.580	2015 Jan 24	MMTO	3400-8400	8	12.8	1.3	Feige34	1.0	3×900
WD0554-165	2015 Jan 24	MMTO	3400-8400	8	12.8	1.5	Feige34	1.0	3×900
SDSSJ072752.76+321416.1	2015 Jan 24	MMTO	3400-8400	8	-93.5	1.0	Feige34	1.0	3×900
SDSSJ081508.78+073145.7	2013 Jul 07 ^e	GEMINI-S	3500-6360	12	0.0	1.3	GD71/Feige110	1.5	6×1500
SDSSJ081508.78+073145.7	2015 Jan 24	MMTO	3400-8400	8	9.3	1.1	Feige34	1.0	4×900
SDSSJ102430.93-003207.0	2013 Feb 15	GEMINI-S	3500-6360	12	0.0	1.3	Feige110	1.5	6×1500
SDSSJ111059.43-170954.1	2015 Jan 24	MMTO	3400-8400	8	-5.2	1.5	Feige34	1.0	3×900
SDSSJ111059.43-170954.1	2015 May 18	GEMINI-S	3500-6500	8	0.0	1.2	Feige67	1.0	8×700
SDSSJ111127.30+395628.0	2015 Jan 24	MMTO	3400-8400	8	-111.6	1.0	Feige34	1.0	3×900
SDSSJ111127.30+395628.0	2015 May 18	MMTO	3400-8400	8	130.0	1.0	BD+284211	1.0	2×900
SDSSJ120650.504+020143.810	2013 Mar 10	GEMINI-S	3500-6360	10	35.0	1.2	Feige110	1.5	6×1500
SDSSJ121405.11+453818.5	2015 Feb 18	GEMINI-N	3520-6360	8	130.0	1.2	Feige34	1.0	6 × 899
SDSSJ121405.11+453818.5	2015 May 18	MMTO	3400-8400	8	1000.0	1.0	BD+284211	1.0	3×900
SDSSJ130234.43+101238.9	2013 Feb 15 ^e	GEMINI-S	3500-6360	10	138.0	1.4	Feige110	1.5	8 × 1200
SDSSJ131445.050-031415.588	2013 Mar 09	GEMINI-S	3500–6360	10	340.0	1.1	Feige110	1.5	6 × 1500
SDSSJ131445.050-031415.588	2015 Jan 24	MMTO	3400–8400	8	-22.4	1.3	Feige34	1.0	4×900
SDSSJ131445.050-031415.588	2015 May 18	MMTO	3400–8400	8	6.4	1.2	BD+284211	1.0	2 × 900
SDSSJ151421.27+004752.8	2013 Mar 10 ^e	GEMINI-S	3500–6360	10	0.0	1.3	Feige110	1.5	8 × 1200
SDSSJ15745.40+554609.7	2015 Jan 24	MMTO	3400–8400	8	-113.9	1.2	Feige34	1.0	2×900
SDSSJ155745.40+554609.7	2015 May 18	MMTO	3400–8400	8	-129.8	1.1	BD+284211	1.0	4×900
SDSSJ163800.360+004717.822	2013 May 18 2013 Apr 08	GEMINI-S	3500-6360	10	0.0	1.3	Feige110	1.5	6×1500
SDSSJ163800.360+004717.822	2015 Apr 08 2015 May 18	MMTO	3400-8400	8	22.0	1.2	BD+284211	1.0	4×900
SDSSJ172135.97+294016.0	2013 May 18 2013 Jun 04	GEMINI-S	3500-6360	10	180.0	2.1	Feige110	1.5	6×1500
SDSSJ172135.97+294016.0	2015 Juli 04 2015 May 18	MMTO	3400-8400	8	-77.6	1.1	BD+284211	1.0	4×900
	•			8	0.0	2.0		1.0	6 × 699
SDSSJ181424.13+785402.9	2015 Apr 27	GEMINI-N	3520–6360	8		1.5	Feige34		
SDSSJ181424.13+785402.9	2015 May 18	MMTO	3400-8400		-152.3		BD+284211	1.0	3×900
SDSSJ20372.169-051302.964	2014 Jul 14 ^e	GEMINI-S	3400–6500	10	0.0	1.1	Feige110	1.5	8 × 1500
SDSSJ20372.169-051302.964	2015 Oct 12	MMTO	3400–8400	8	-8.4	1.3	BD+284211	1.25	3 × 1200
SDSSJ210150.65-054550.9	2014 Jul 20	GEMINI-S	3400–6500	10	0.0	1.2	Feige110	1.5	6 × 1300
SDSSJ210150.65-054550.9	2015 May 18	MMTO	3400-8400	8	-39.9	1.5	BD+284211	1.0	2×900
SDSSJ210150.65-054550.9	2015 Oct 11	MMTO	3400–8400	8	1.7	1.3	BD+284211	1.25	6 × 1200
SDSSJ232941.330+001107.755	2015 Oct 01 ^e	GEMINI-N	3520–6360	8	12.0	1.2	BD+284211	1.0	11 × 1099
SDSSJ232941.330+001107.755	2015 Oct 11	MMTO	3400–8400	8	-14.2	1.2	BD+284211	1.25	6×1200
SDSSJ235144.29+355542.6	2015 May 18	MMTO	3400–8400	8	-74.2	1.7	BD+284211	1.0	900 + 765
SDSSJ235144.29+355542.6	2015 Sep 15	GEMINI-N	3520–6360	8	180.0	1.2	BD+284211	1.0	6 × 999
SDSSJ235144.29+355542.6	2015 Oct 11	MMTO	3400-8400	8	126.4	1.0	BD+284211	1.25	5×1200

Notes.

CCD data and optimally extract (Horne 1986) the spectra. The wavelength scale was evaluated via polynomial fits to calibration lamp spectra and we then resampled the WD

spectra onto a linear scale with 1 Å/pixel and 2 Å/pixel for the GMOS and MMT data, respectively. We used our own custom IDL routines to flux calibrate the data (Matheson et al. 2008).

^a Telescope used to obtain given spectrum. GEMINI-N and GEMINI-S denote the use of GMOS at either the northern or southern site for the Gemini Observatory. MMTO denotes the use of the Blue Channel spectrograph at the MMT Observatory.

^b Resolution of the spectrum as determined from the full-width at half maximum of sky lines present in the two-dimensional spectrum. This is, in general, an upper limit as the resolution for the stellar spectrum is determined by the seeing and the slit width. In many cases, especially with the wider slits used with GMOS, the resolution of the spectrum is better than this reported value.

^c The position angle of the observations. Spectra from the MMT were typically observed at the parallactic angle, while the Gemini data were not.

d Flux standards used to calibrate the data: Feige 34, BD+28°4211, Feige 110, —(Stone 1977; Massey et al. 1988; Massey & Gronwall 1990); GD71—(Bohlin et al. 1995); G191B2B—(Oke 1974; Massey et al. 1988).

^e Spectra from Gemini were obtained in queue mode and thus could be observed over multiple nights. The UT date reported for these stars is represents an average of the actual dates. Note that observations for SDSSJ081508 were separated by 10 months.

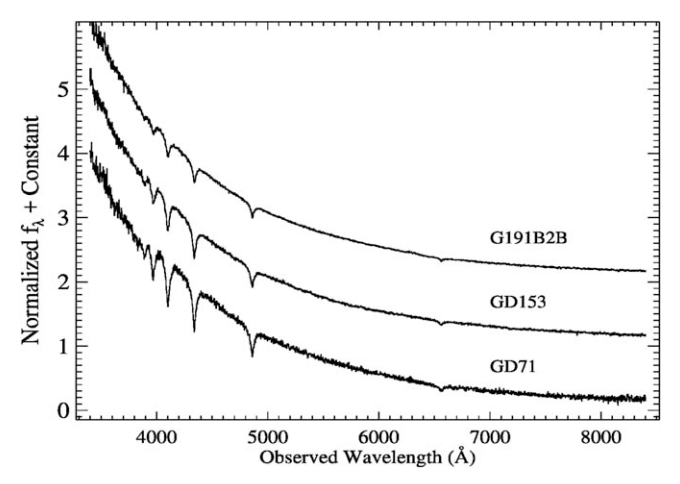


Figure 12. Spectra of the three HST primary CALSPEC standards.

The standard stars for each spectrum are listed in Table 5. The spectra of our DAWDs are shown in three figures. Figure 12 shows the spectra of the three primary CALSPEC standards. The spectra of stars obtained at Gemini are shown in Figure 13 while those obtained at the MMT are shown in Figure 14. The details of the determination of $T_{\rm eff}$ and $\log g$ will be described in a forthcoming analysis paper (Narayan et al. 2018, in preparation).

One of the WD stars showed indications of abnormality in its spectra. SDSSJ20372.169–051302.964 was observed over several nights with GMOS-S. There is a narrow emission feature present in the cores of the Balmer absorption lines. The emission feature moves relative to the broader line. This may be the result of a low-luminosity companion or some other activity associated with the WD. Thus, this star is unsuitable for use as a spectrophotometric standard because the model spectra only apply to single, inactive DAWDs.

7. Setting the Photometric Reference System

The photometry for our candidate spectrophotometric standards needs to be placed on a common flux scale at the top of the atmosphere. To achieve this goal, we observed the three *HST* primary CALSPEC WDs and the candidate DAWDs by using the same instrument and telescope set-up in Cycle 22. These observations allowed us to determine the instrumental ZPs for each WFC3 filter and to tie the magnitudes of all of the targets to the same photometric system.

As a first step, we calculated fluxes and magnitudes in the AB photometric system for the *HST* primary CALSPEC WDs by using the *HST* tool *Pysynphot*. ¹⁶ For these simulations, we used the latest model spectra of the three DAWDs provided by the CALSPEC database (mod_010), which are calculated with the Non-Local Thermal-Equilibrium code from Rauch et al. (2013). These models are normalized to an absolute flux level, as defined by the flux of $3.44 \times 10^{-9} \, \mathrm{erg \, cm^{-2} \, s^{-1} \, \mathring{A}^{-1}}$ for Vega at $0.5556 \, \mu \mathrm{m}$, as reconciled with the *MSX* mid-IR absolute flux measures (B14).

The AB magnitude system (Oke 1974) is defined for monochromatic fluxes. If the flux at frequency ν is denoted by f_{ν} and expressed in units of erg cm⁻² s⁻¹ Hz⁻¹, then the

corresponding AB magnitude at ν is defined by:

$$m(AB_{\nu}) = -2.5 \log(f_{\nu}) - 48.60.$$
 (3)

This corresponds to a normalization where an object with a flat spectrum has AB magnitude equal to its V band magnitude (Oke & Gunn 1983).

To incorporate the idea of AB magnitudes for non-monochromatic use, say for a passband X, we use the extension as proposed by Fukugita et al. (1996) for a photon proportional detector system to define the quantity f_X :

$$f_X = \frac{\int f_{\nu} v^{-1} R d\nu}{\int \nu^{-1} R d\nu} = \frac{\int N_{\nu} R d\nu}{\int (h\nu)^{-1} R d\nu}$$
(4)

where R is the (telescope + instrument + filter) response function for passband X, N_{ν} is the count rate of photons per unit frequency and h is Planck's constant. The numerator on the rightmost side is the photon count rate in the band, so f_X is directly proportional to the photon count rate.

The AB magnitude for passband *X* is then given by:

$$m(AB_X) = -2.5 \log(f_X) - 48.60.$$
 (5)

A characteristic wavelength, *pivot wavelength*, is defined to transform flux densities from the frequency to the wavelength domain as:

$$\lambda_p = \sqrt{\frac{cf_\nu}{f_\lambda}} = \sqrt{\frac{\int R\lambda d\lambda}{\int R\frac{d\lambda}{\lambda}}} \tag{6}$$

which is a source independent quantity. The Space Telescope (ST) magnitude system is defined in the wavelength domain for passband *X* as:

$$m(ST_X) = -2.5\log(f_X) - 21.10 \tag{7}$$

where ST mag = 0 is 3.63×10^{-9} erg cm⁻² s⁻¹ Å⁻¹. Having defined λ_p , we can then convert AB to ST magnitudes with the relation:

$$m(ST_{\lambda}) = m(AB_{\nu}) + 5\log(\lambda_{p}) - 18.70.$$
 (8)

We used *Pysynphot* to calculate synthetic fluxes and magnitudes in the AB photometric system for the primary WDs. As a reference, we used the most updated files available on the Space Telescope database. These reference files give the transmission curves for every element in the optical path of the (*HST* + WFC3 + filter) system. For a complete list of the reference files, please see the linked web-page. The AB fluxes and magnitudes obtained for the three *HST* primary CALSPEC WDs are listed in Table 6.

The derived AB synthetic magnitudes are compared to the instrumental magnitudes measured from our observations in Cycle 22 for the primary WDs. Figure 15 shows the difference between synthetic and instrumental magnitudes as a function of the observing epoch for the three stars. Observations were divided in multiple exposures for a total of three visits per star in a time interval of ~ 1.3 yr. We performed a 1.5σ clipping on the data and we estimated the biweight mean of the difference for the three primary WDs. This difference sets the ZP for our observations. The estimated ZPs with their errors are labeled in each panel of Figure 15. For observations in the F275W and F336W filters, GD71 measurements (black dots) are

http://pysynphot.readthedocs.io/en/latest/using_pysynphot.html

¹⁷ http://www.stsci.edu/hst/observatory/crds/throughput.html

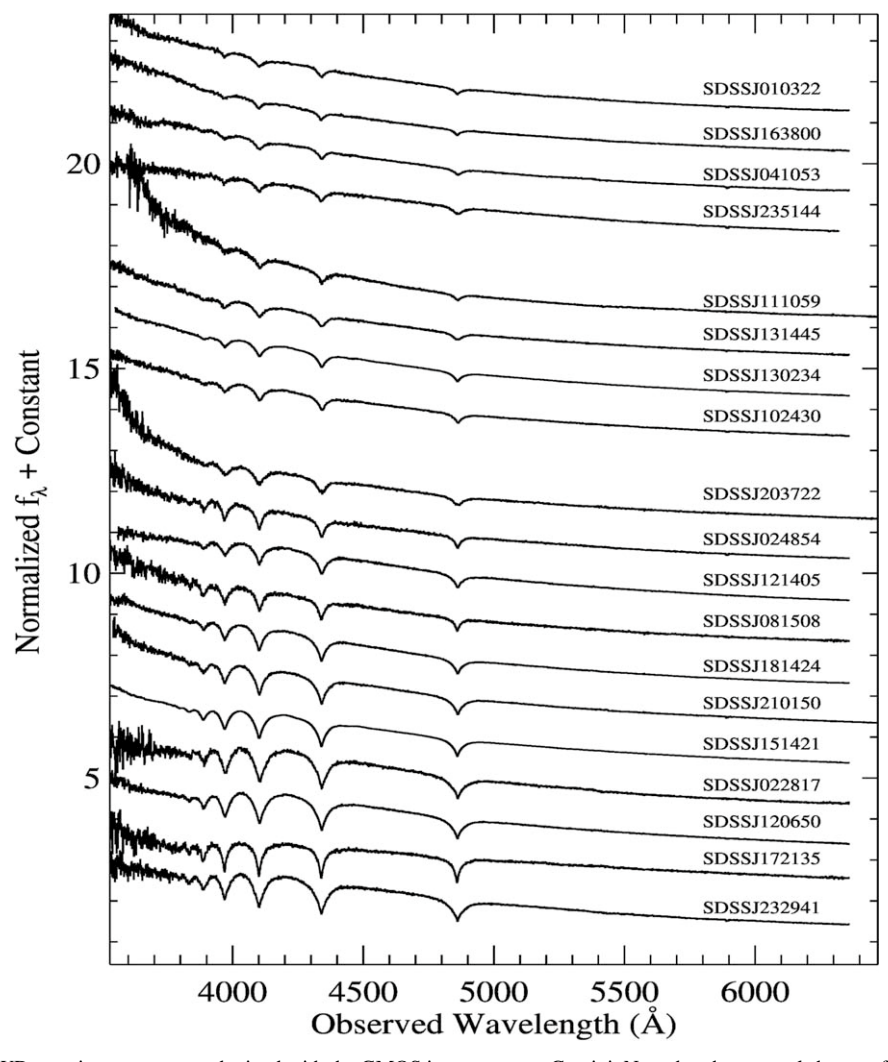


Figure 13. Spectra of the DAWD stars in our program obtained with the GMOS instruments at Gemini. Note that the unusual shapes of some of the spectra are caused by atmospheric dispersion effects and slit losses. Spectra are ordered by $T_{\rm eff}$, with the hottest stars at the top.

consistently offset; i.e., fainter, compared to the other two WDs (cyan stars and magenta triangles). The cause of this difference is not clear. A set of ZPs for each of the photometric reduction method was estimated and they are listed in Table 7.

As a sanity check we also derived ZPs for the same filters but for an aperture radius of 10 pixels for WFC3-UVIS, and to infinity for WFC3-UVIS and WFC3-IR; i.e., the aperture radii used by the WFC3 team to provide the official ZPs. To derive ZPs to infinity we used the encircled energy correction tables provided by the WFC3 database. ¹⁸

Figure 16 shows the comparison between WFC3 official ZPs and the ZPs measured using our observations, reduced with DAOPHOT, for the three CALSPEC standards as a function of wavelength. Error bars show uncertainties in our ZP estimates because there are no errors provided for the WFC3 ZPs. The left-hand panel shows the comparison for ZPs derived for an aperture radius of 10 pixels (F160W is excluded because ZPs for WFC3-IR are not provided for this aperture), while the right panel shows the same comparison for all filters and for an infinite aperture radius. The two sets of ZPs agree very well, with only the F275W and the F160W filters being ≥1% off.

WFC3 official ZPs are calculated by using a set of observations taken between 2009 and 2015: the epoch to which these sensitivities are normalized is then \approx 2012.5, and they are an average of measurements collected on the UVIS2 amplifiers C and D. The WFC3 inverse sensitivities change with time. Our ZPs are provided for the average epoch of the observations, i.e., \approx 2015.5, and they are based on data collected only on amplifier C. The change in sensitivity of the (detector+filter) system will be analyzed in Section 7.1. In spite of these issues, the overall average difference between the two sets of ZP is 0.003 mag with a dispersion of 0.005 mag for a 10 pixel aperture, and 0.002 mag with a dispersion of 0.006 mag for the infinite aperture. The ZPs for a 10 pixel aperture radius and for infinity are listed in Table 8. These ZPs can be used by any astronomer performing observations by using WFC3-UVIS2 and WFC3-IR. They can also be used to tie their photometry to the *HST* photometric scale.

7.1. Tracking WFC3 Sensitivity Variation with Time

We used observations of the three *HST* primary CALSPEC standards to track the variation of WFC3 sensitivity as a function of filter and time. The observations of the CALSPEC stars span a time interval of approximately 1.3 yr, from the fall

¹⁸ http://www.stsci.edu/hst/wfc3/analysis/ir_ee; http://www.stsci.edu/hst/wfc3/analysis/uvis_ee

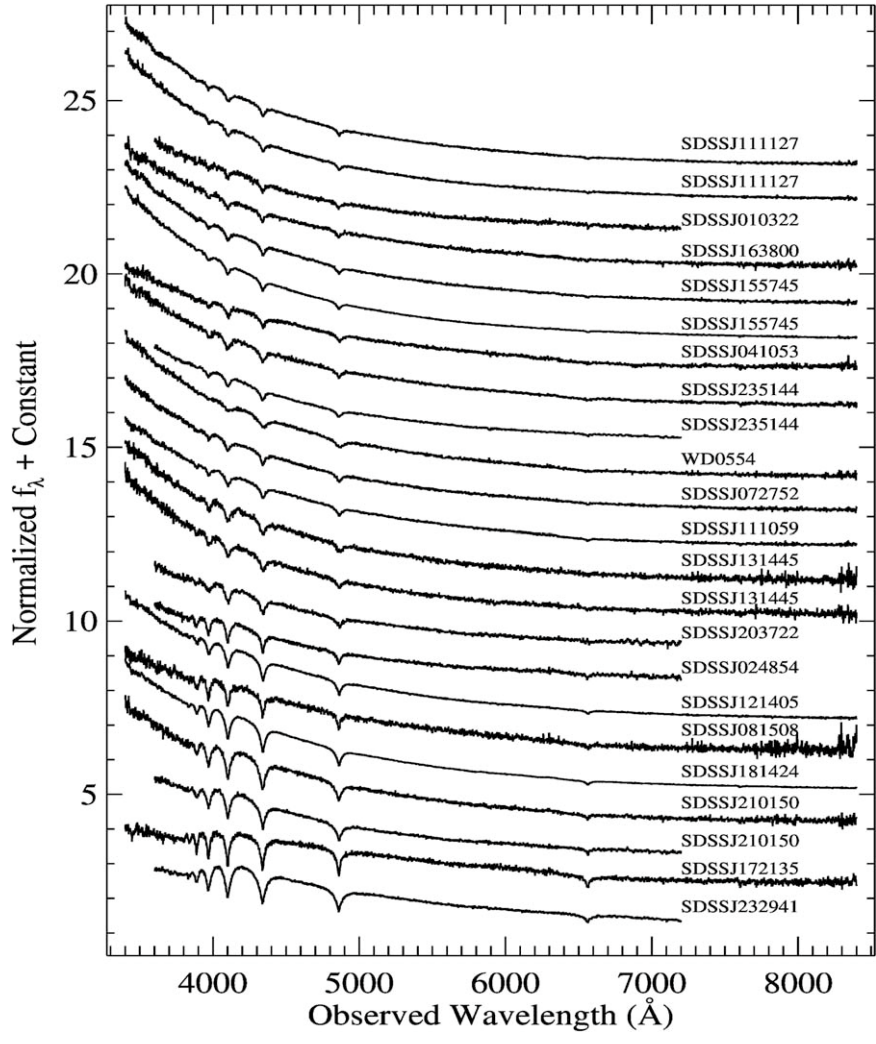


Figure 14. Spectra of the WD stars in our program obtained with the Blue Channel spectrograph at the MMT. Spectra are ordered by $T_{\rm eff}$, with the hottest stars at the top.

of 2014 to the beginning of 2016. Instrumental count rates for aperture radii 7.5 (WFC3-UVIS) and 5 (WFC3-IR) pixels in the AB photometric system were derived for the CALSPEC WDs in the six filters for the three different visits, each one with a number of observations ranging from six to eight, depending on the filter; as described in Section 3. Synthetic count rates were derived with *Pysynphot* for the same stars as observed with WFC3. We followed the same procedure described in Section 7 and we simulated count rates for aperture radii of 7.5 (WFC3-UVIS) and 5 (WFC3-IR) pixels; i.e., the radii that we used to perform photometry on the real images.

Figure 17 shows the ratio of the observed to synthetic count rates as a function of the observing epoch for the three primary WDs (GD71 = black dots, GD153 = cyan stars, and G191B2B = magenta triangles) and the six filters, after we performed a 1.5σ clipping of the data. The plot shows that the sensitivity decreases with time for all filters: the decrease is steeper for the bluer filters, F275W, F336W, and F475W; and it is shallower for the redder filters, F625W, F775W, and F160W. We performed a linear least-square fit and obtained slopes ranging from -0.03 to -0.27, with the larger slopes for

F336W and F475W and the smaller for F625W and F160W. The fit to the data and the final sensitivity decrease rate per year are shown in Figure 17.

The sensitivity loss rates that we obtained from our observations are in good agreement, within uncertainties, with the rates provided by the WFC3 photometric contamination monitor studies. One of the contamination monitor programs is based on about 8 yr of observations of the CALSPEC WD GWR70. These data show that WFC3 sensitivity decreases by less than 0.01% for the UV filters F275W and F336W (see Table 4 of Shanahan et al. 2017 for more details). However, no measurements are available for the F475W, F625W and F775W filters from this contamination monitor. It is worth mentioning that UV filters had an increase in sensitivity soon after WFC3 was installed and they then started to decrease (see Figure 8 in Shanahan et al. 2017). The very low percentage decrease obtained by Shanahan et al. (2017) for the UV filters is due to fitting all of the measurements for GWR70 at the same time. A more recent contamination monitor study from the WFC3 team that was based on 8 yr of photometry for the three primary WDs and the CALSPEC G-type standard P330E was able to obtain steeper slopes for the UV filters by only

Table 6
Synthetic Magnitudes and Fluxes in the AB and ST Photometric System for the Three HST Primary CALSPEC DAWDs as Simulated by Using Pysynphot

Filter	λ_p	AB mag	F_{ν}	ST mag	F_{λ}
			(erg cm ⁻²		(erg cm ⁻²
	(Å)	(mag)	$s^{-1} Hz^{-1}$)	(mag)	s ⁻¹ Hz ⁻¹)
			GD153		
F275W	2703	12.200	4.78e-25	10.669	1.96e-13
F336W	3354	12.566	3.41e - 25	11.503	9.09e - 14
F475W	4770	13.098	2.09e - 25	12.799	2.76e - 14
F625W	6240	13.598	1.32e - 25	13.882	1.02e - 14
F775W	7651	14.004	9.09e - 26	14.730	4.66e - 15
F160W	15,369	15.414	$2.48e{-26}$	17.654	3.15e-16
			GD71		
F275W	2703	11.981	5.85e-25	10.450	2.40e-13
F336W	3354	12.327	4.26e - 25	11.264	$1.13e{-13}$
F475W	4770	12.794	2.77e - 25	12.496	3.64e - 14
F625W	6240	13.275	1.78e - 25	13.558	1.37e - 14
F775W	7651	13.672	1.23e-25	14.398	6.32e - 15
F160W	15,369	15.060	3.43e - 26	17.301	4.36e-16
			G191B2B		
F275W	2703	10.492	2.30e-24	8.960	9.46e-13
F336W	3354	10.892	1.60e - 24	9.829	4.25e - 13
F475W	4770	11.500	9.12e - 25	11.201	1.20e-13
F625W	6240	12.030	5.60e - 25	12.314	4.31e - 14
F775W	7651	12.449	3.81e - 25	13.175	1.95e - 14
F160W	15,369	13.885	1.01e-25	16.125	$1.29e{-15}$

Note. The pivot wavelength for each filter is also listed. See text for more details

considering measurements from when the sensitivity started to decrease. The new sensitivity loss rates range from \sim -0.05 to -0.2% per year for the UVIS filters F275W, F336W, F475W, F625W, and F775W (Khandrika et al. 2018). These results will soon published be in a WFC3 ISR.

The WFC3 sensitivity loss rates that we derived by using our observations of the primary WDs have very large errors, 0.1%–0.2%. Our data cover a very short time interval of a little more than 1 yr and they are insufficient to fully characterize the sensitivity variations with time. Meanwhile, the total dispersion of the measurements for the three primary WDs is always less than ~ 0.005 mag in all UVIS filters and less then 1% for in the infrared in the considered time interval of our program observations. Therefore, we did not apply any time correction to the photometry.

7.2. The Final Magnitudes

The ZPs obtained in Section 7 were applied to the weighted mean instrumental magnitudes of all the 23 candidate standard DAWDs. The ZPs were derived by using observations of the three *HST* primary CALSPEC standards, performed under the same conditions, and reduced with the same technique. Therefore, they take into account any possible systematics in the observations and data reduction process. For each of the three different reduction methods, final calibrated magnitudes for filter *X* in the AB photometric system are derived as:

$$m(AB_X)_{cal} = m(AB_X)_{inst} + ZP_{AB_X}$$

= $(-2.5 \log(f_X) - 48.60) + ZP_{AB_X}$ (9)

where f_X is in electrons/s, for aperture radii of 7.5 (WFC3-UVIS) and 5 pixels (WFC3-IR), respectively, and ZP_{AB_X} are the estimated ZPs listed in Table 7.

The final magnitudes for the 23 candidate spectrophotometric standard DAWDs and the HST primary CALSPEC WDs are listed in Table 9. Figure 3 shows the Bp - Rp, F475W – F775W color–color diagram for the 23 candidate spectrophotometric standard DAWDs, where GAIA and WFC3 magnitudes derived with DAOPHOT are plotted.

Regardless of the photometric reduction method used, the magnitudes for our DAWDs have an average dispersion ranging from 1 to 3 milli-mag for the WFC3-UVIS filters and from 5 to 10 milli-mag for the F160W IR filter.

8. Summary and Conclusions

In this paper, we presented the methods used to provide subpercent precision photometry for a set of faint candidate spectrophotometric standard DAWDs. We also presented data reduction processes and possible sources of uncertainties of the spectroscopic data collected for the same stars. These spectra are used to derive temperature and surface gravities for the candidate standards.

To investigate the possible sources of systematics and to derive reliable uncertainties for the DAWD photometry, we used three different software packages to reduce WFC3 data: DAOPHOT, ILAPH, and SExtractor. Our analysis showed that photometry performed with the first two packages agrees very well within uncertainties. Meanwhile, photometry from SExtractor shows larger dispersion and a trend where the magnitudes of fainter stars are fainter when compared to DAOPHOT and ILAPH magnitudes, particularly in the bluest filters: F275W and F336W. This trend is probably due to SExtractor over-estimating the sky background.

We tested our data for photometric uncertainties due to the presence of external or internal persistence on the IR images. We found that the largest fraction of pixels affected by a persistence signal higher than $0.01\,\mathrm{e^-\,s^{-1}}$ is 0.33%, for images of star SDSSJ181424.075+785403.048. However, the affected pixels do not overlap with the location of the star on the images. Our observing strategy was devised to avoid self-persistence in our exposures.

CRNL in WFC3-IR exposures was estimated to be 0.010 ± 0.0025 mag per dex, which might slightly affect our observations. However, we do not apply any CRNL corrections on the photometry presented here and we plan to fully characterize this effect in NA19.

Our data show no systematics in the photometry due to the WFC3-UVIS shutter shading effect for an aperture radius of 7.5 pixels. We tested photometry on 1 s exposures for G191B2B and we found that the dispersion of the measurements on images collected by using shutter blade B, $\sigma=0.004$ mag, is about the same when compared to the dispersion on images observed with blade A, $\sigma=0.005$ mag. All the other DAWDs were observed with exposure times $\gtrsim 5$ s. Consequently, our observations are not affected by shutter shading.

The presence of unseen companion stars could also introduce uncertainties/systematics in the photometry. However, the observed DAWDs are all in very sparse fields, with a maximum of three other objects, including the DAWD in the $\sim\!20\times20''$ observed FoV down to $g\sim23$ mag. Our simulations also showed that stars fainter than 6 mag compared to the

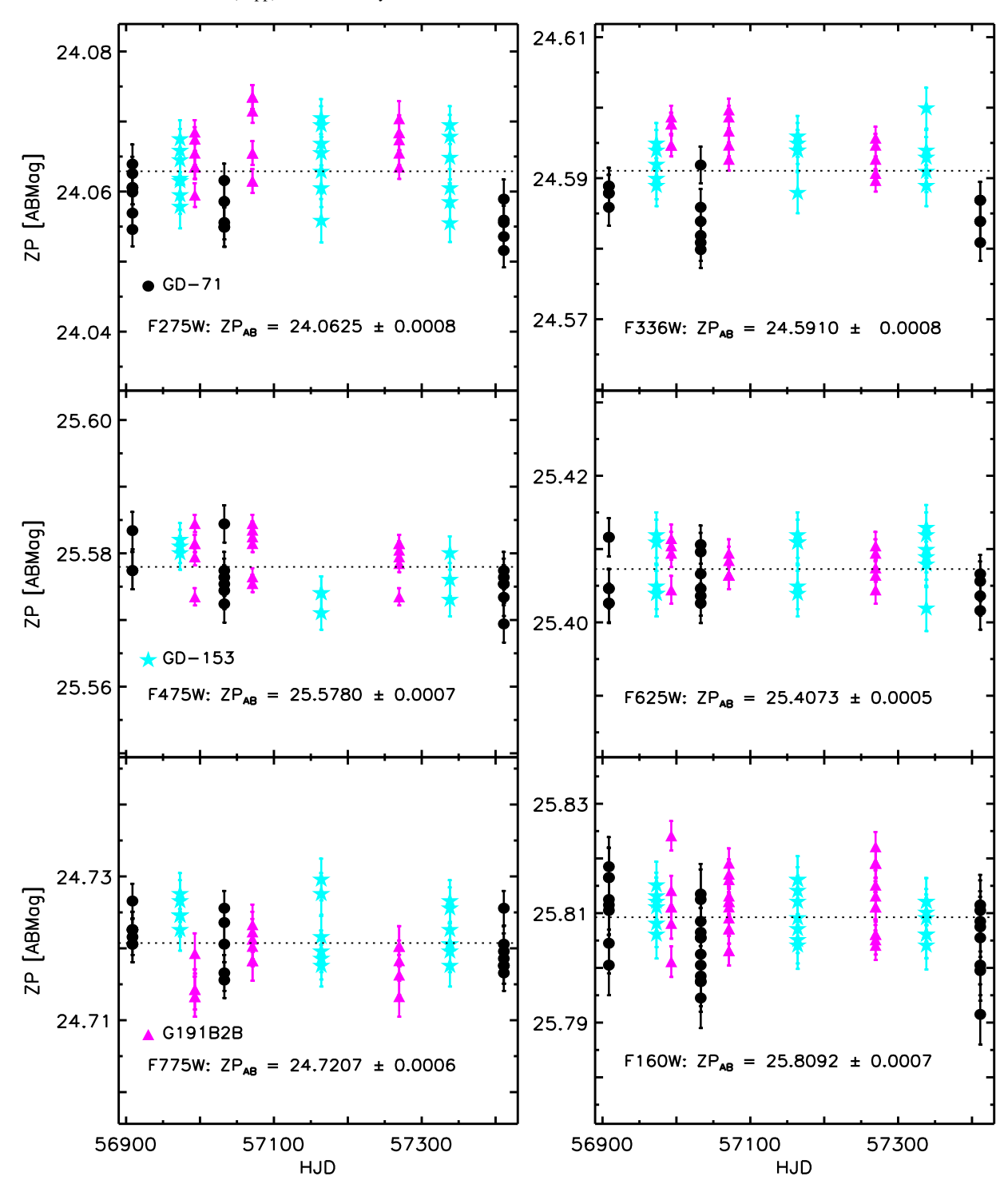


Figure 15. ZPs in the AB photometric system based on all the observations for the three *HST* primary CALSPEC WDs (GD71 = black dots, GD153 = cyan stars, and G191B2B = magenta triangles) as a function of the Heliocentric Julian date (HJD) for six WFC3-UVIS and WFC3-IR filters as measured with DAOPHOT. Error bars are shown and the derived ZPs are labeled.

target WDs cannot affect the photometry of the target DAWD, even if they fall inside the aperture radius. Therefore, we can safely assume that the photometry of our set of standards cannot be contaminated by unseen neighbor stars.

Time-series observations collected with the LCO network of telescopes showed that most of our candidate spectrophotometric standards are stable. Two of them—namely

SDSSJ20372.169–051302.964 and WD0554–165—show clear signs of variability in their light curves. The first star also shows emission features in the Balmer lines of the spectra, which implies the presence of a low-mass companion. We do not know the origin of the variability for WD0554–165. Two other DAWDs—SDSSJ010322.10–002047.7 and SDSSJ102430.93–003207.0—show hints of variability, but

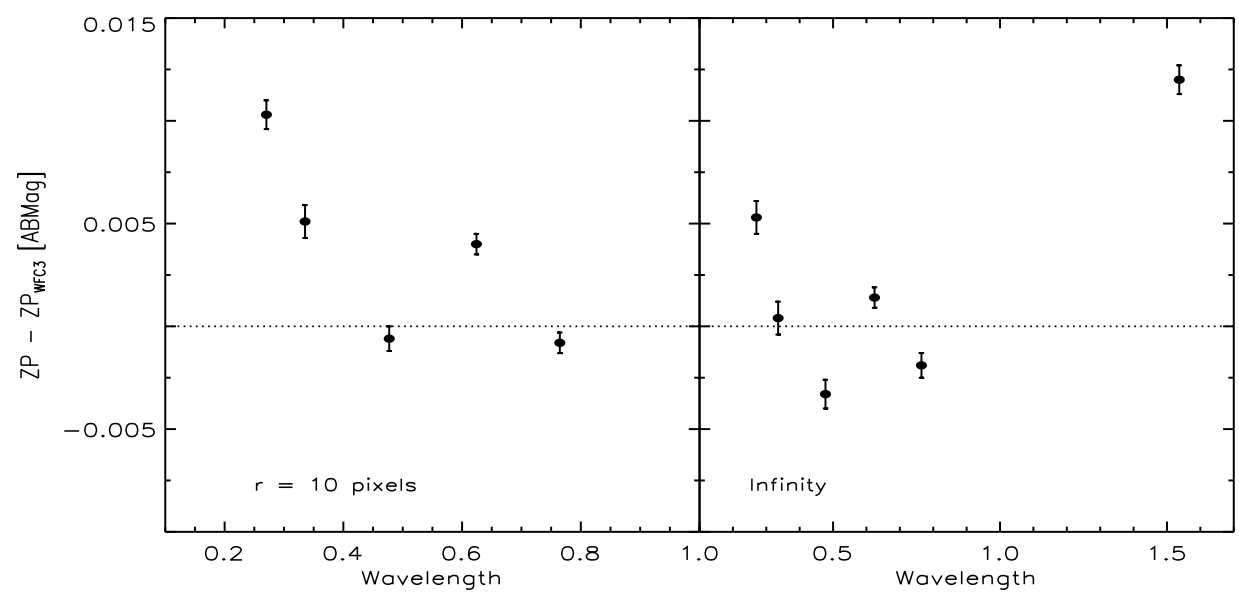


Figure 16. Comparison between ZPs in the AB photometric system measured from our observations of the three HST primary CALSPEC WDs and the WFC3 official ZPs as a function of wavelength. The ZPs are derived for an aperture radius of 10 pixels (left panel, UVIS) and infinity (right, UVIS + IR). See text for more details.

Table 7
Zero Points and their Uncertainties for WFC3-UVIS (Aperture Radius r = 7.5 pixels) and IR (r = 5 pixels) Observations in the AB Photometric System

Filter	ZP (DAOPHOT) (mag)	eZP (DAOPHOT) (mag)	ZP (ILAPH) (mag)	eZP (ILAPH) (mag)	ZP (Sextractor) (mag)	eZP (Sextractor) (mag)
F275W	24.0612	0.0008	24.0596	0.0009	24.0594	0.0009
F336W	24.5910	0.0008	24.5899	0.0008	24.5889	0.0010
F475W	25.5780	0.0007	25.5774	0.0009	25.5761	0.0007
F625W	25.4073	0.0005	25.4056	0.0007	25.4043	0.0005
F775W	24.7207	0.0006	24.7189	0.0008	24.7171	0.0006
F160W	25.8092	0.0007	25.8116	0.0009	25.8106	0.0007

Note. Zero points are derived by using observations of the three HST primary calspec standards as measured with three different methods.

Table 8

Zero Points and their Uncertainties for 10 pixel Aperture Radius (WFC3-UVIS) and Infinity (WFC3-UVIS, WFC3-IR) in the AB Photometric System

Filter	ZP ₁₀ (mag)	eZP ₁₀ (mag)	ZP _{inf} (mag)	eZP _{inf} (mag)	ZP ₁₀ (WFC3) (mag)	ZP _{inf} (WFC3) (mag)
F275W	24.0853	0.0007	24.2293	0.0008	24.075	24.224
F336W	24.6131	0.0008	24.7344	0.0008	24.608	24.734
F475W	25.6034	0.0006	25.7057	0.0007	25.604	25.709
F625W	25.4310	0.0005	25.5334	0.0005	25.427	25.532
F775W	24.7522	0.0005	24.8571	0.0006	24.753	24.859
F160W			25.9580	0.0007		25.946

Note. Zero points are derived by using our observations of the three *HST* primary CALSPEC standards as measured with DAOPHOT (first columns) and the official WFC3 values are in the last two columns (Current WFC3 UVIS and IR official ZPs can be found at http://www.stsci.edu/hst/wfc3/phot_zp_lbn).

these results need to be confirmed with further data. SDSSJ20372.169–051302.964 and WD0554–165 will be excluded from our set of candidate standard DAWDs.

We used observations of the three *HST* primary CALSPEC standards, which were collected at the same time as our target DAWDs, to estimate ZPs in the AB photometric system to be applied to instrumental magnitudes of all the observed targets.

We also derived ZPs in the AB photometric system for six WFC3 filters—namely F275W, F336W, F475W, F625W, F775W and F160W—for a 10 pixel aperture radius and for

infinity. The ZPs are provided in Table 8 and they can be used to calibrate any WFC3-UVIS2 photometry.

We also verified for the presence of WFC3 sensitivity changes during the \sim 1.3 yr of the observations by using the same data. A decrease in sensitivity is observed in all six filters, with the largest percentage decline in sensitivity for F475W (-0.27%) and the smallest for F625W and F160W (-0.03%). Although our data do not span a sufficient time interval to fully characterize WFC3 sensitivity behavior, the overall dispersion of the measurements over the time interval of our observations

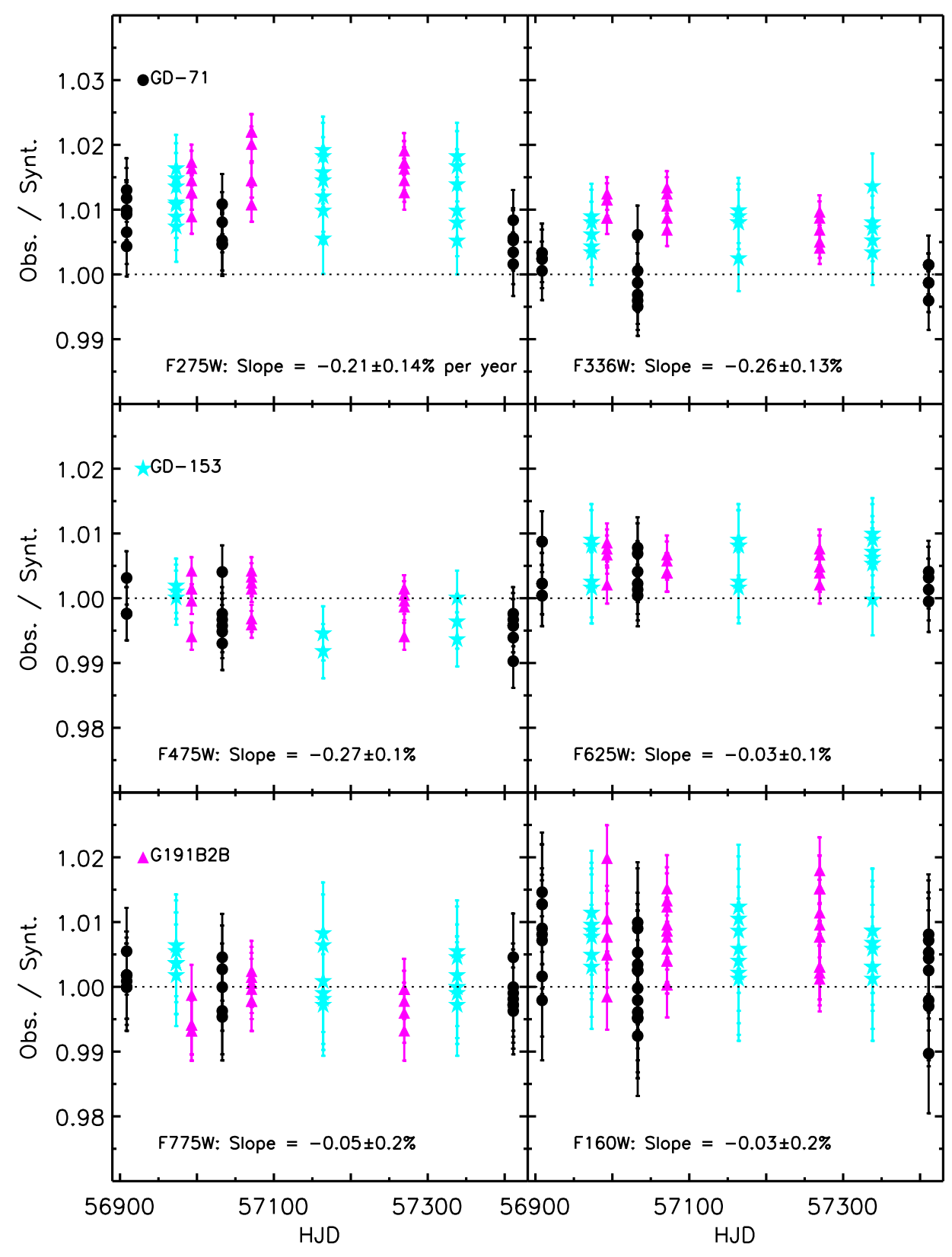


Figure 17. Ratio of observed to synthetic count rates for the three *HST* primary CALSPEC standards (GD71 = black dots, GD153 = cyan stars, and G191B2B = magenta triangles) as a function of the Heliocentric Julian date (HJD) for six WFC3-UVIS and WFC3-IR filters. Error bars and the slope fits are shown. The rate of yearly sensitivity loss is labeled.

is less than 0.5% for WFC3-UVIS and less than 1% for WFC3-IR. Therefore, we do not apply any time correction to our photometry.

We provided final calibrated AB magnitudes in five WFC3-UVIS filters and one IR filter for the 23 candidate spectro-photometric standard DAWDs and the three *HST* primary

 Table 9

 Photometry in the WFC3 UVIS and IR Filters for the 3 HST Primary CALSPEC Standards and the 23 Candidate Standard DAWDs in the AB Photometric System

Star	F275W	dF275W	F336W	dF336W	F475W	dF475W	F625W	dF625W	F775W	dF775W	F160W	dF160W
	(mag)	(mag)	(mag)	(mag)	(mag)	(mag)	(mag)	(mag)	(mag)	(mag)	(mag)	(mag)
					DAOPHC	T						
Offsets			-0.033	0.001	-0.007	0.005	-0.006	0.004	0.013	0.006	-0.014	0.004
G191B2B	10.488	0.002	10.888	0.001	11.498	0.001	12.030	0.001	12.451	0.001	13.883	0.002
GD71	11.986	0.002	12.333	0.001	12.796	0.001	13.277	0.001	13.672	0.001	15.065	0.002
GD153	12.199	0.002	12.565	0.001	13.099	0.002	13.597	0.001	14.002	0.001	15.413	0.002
SDSSJ010322.19-002047.7	18.191	0.004	18.524	0.006	19.082	0.005	19.562	0.005	19.967	0.005	21.364	0.020
SDSSJ022817.16-082716.4	19.512	0.006	19.732	0.037	19.811	0.005	20.178	0.006	20.506	0.007	21.737	0.015
SDSSJ024854.96+334548.3	17.829	0.004	18.042	0.004	18.367	0.003	18.745	0.002	19.078	0.002	20.341	0.006
SDSSJ041053.632-063027.580	18.110	0.009	18.401	0.004	18.879	0.004	19.254	0.003	19.387	0.007	19.500	0.005
WD0554–165	16.774	0.005	17.150	0.003	17.720	0.005	18.221	0.002	18.622	0.007	20.046	0.002
SDSSJ072752.76+321416.1	17.158	0.003	17.467	0.003	17.990	0.003	18.456	0.002	18.839	0.002	20.214	0.006
SDSSJ081508.78+073145.7	18.939	0.005	19.262	0.006	19.713	0.004	20.186	0.004	20.578	0.005	21.967	0.015
SDSSJ102430.93-003207.0	18.248	0.038	18.509	0.004	18.903	0.004	19.314	0.005	19.667	0.009	20.989	0.014
SDSSJ111059.42-170954.2	17.039	0.004	17.351	0.004	17.864	0.002	18.313	0.002	18.690	0.002	20.057	0.005
SDSSJ111127.30+395628.0	17.432	0.004	17.832	0.005	18.419	0.003	18.940	0.004	19.344	0.002	20.795	0.010
SDSSJ120650.504+020143.810	18.236	0.004	18.484	0.004	18.669	0.004	19.058	0.004	19.411	0.005	20.700	0.011
SDSSJ121405.11+453818.5	16.938	0.002	17.279	0.002	17.758	0.002	18.231	0.002	18.630	0.002	20.035	0.004
SDSSJ130234.43+101238.9	16.185	0.002	16.519	0.002	17.033	0.002	17.512	0.002	17.904	0.001	19.302	0.004
SDSSJ131445.050-031415.588	18.254	0.004	18.593	0.004	19.100	0.004	19.571	0.004	19.933	0.010	21.329	0.012
SDSSJ151421.27+004752.8	15.108	0.002	15.387	0.002	15.707	0.002	16.119	0.001	16.470	0.001	17.783	0.004
SDSSJ155745.40+554609.7	16.496	0.002	16.873	0.002	17.468	0.003	17.990	0.002	18.389	0.002	19.832	0.005
SDSSJ163800.360+004717.822	18.012	0.007	18.314	0.004	18.838	0.004	19.283	0.003	19.664	0.005	20.999	0.015
SDSSJ172135.97+294016.0	20.370	0.010	20.086	0.014	19.654	0.004	19.670	0.003	19.769	0.003	20.554	0.022
SDSSJ181424.075+785403.048	15.788	0.002	16.119	0.002	16.542	0.002	17.004	0.002	17.392	0.001	18.782	0.002
SDSSJ203722.169-051302.964	18.254	0.007	18.540	0.004	18.940	0.006	19.371	0.007	19.674	0.008	20.965	0.009
SDSSJ210150.65-054550.9	18.064	0.003	18.328	0.004	18.654	0.003	19.062	0.002	19.419	0.003	20.737	0.006
SDSSJ232941.330+001107.755	17.940	0.003	18.105	0.004	18.158	0.005	18.472	0.003	18.785	0.006	19.997	0.007
SDSSJ235144.29+375542.6	17.446	0.003	17.658	0.002	18.073	0.002	18.459	0.002	18.788	0.002	20.070	0.004
					SExtracto	or						
Offsets			-0.031	0.003	-0.004	0.003	-0.009	0.002	0.012	0.004	-0.011	0.005
G191B2B	10.488	0.002	10.889	0.001	11.497	0.001	12.029	0.001	12.451	0.001	13.884	0.001
GD71	11.989	0.002	12.335	0.001	12.798	0.001	13.277	0.001	13.671	0.001	15.063	0.002
GD153	12.196	0.002	12.562	0.001	13.097	0.002	13.598	0.001	14.003	0.001	15.414	0.002
SDSSJ010322.19-002047.7	18.197	0.004	18.532	0.005	19.088	0.005	19.564	0.004	19.968	0.005	21.359	0.010
SDSSJ022817.16-082716.4	19.531	0.006	19.761	0.018	19.823	0.006	20.178	0.005	20.514	0.004	21.740	0.013
SDSSJ024854.96+334548.3	17.840	0.003	18.047	0.004	18.368	0.003	18.745	0.002	19.079	0.002	20.335	0.005
SDSSJ041053.632-063027.580	18.109	0.009	18.410	0.004	18.884	0.004	19.256	0.003	19.387	0.005	19.500	0.005
VD0554-165	16.777	0.005	17.153	0.004	17.729	0.003	18.222	0.003	18.619	0.005	20.043	0.006
SDSSJ072752.76+321416.1	17.164	0.003	17.474	0.003	17.993	0.002	18.457	0.002	18.840	0.002	20.214	0.005
SDSSJ081508.78+073145.7	18.965	0.007	19.280	0.005	19.714	0.005	20.185	0.004	20.579	0.005	21.967	0.012
SDSSJ102430.93-003207.0	18.264	0.014	18.517	0.004	18.909	0.004	19.314	0.003	19.668	0.008	20.994	0.010
SDSSJ111059.42-170954.2	17.047	0.003	17.359	0.004	17.867	0.002	18.314	0.002	18.689	0.002	20.054	0.005
SDSSJ111127.30+395628.0	17.437	0.004	17.838	0.005	18.424	0.003	18.940	0.004	19.346	0.002	20.790	0.008
SDSSJ120650.504+020143.810	18.244	0.004	18.491	0.004	18.672	0.004	19.060	0.003	19.412	0.004	20.703	0.006

Calamida et al

Table 9 (Continued)

Star	F275W (mag)	dF275W (mag)	F336W (mag)	dF336W (mag)	F475W (mag)	dF475W (mag)	F625W (mag)	dF625W (mag)	F775W (mag)	dF775W (mag)	F160W (mag)	dF160W (mag)
SDSSJ121405.11+453818.5	16.943	0.003	17.283	0.002	17.759	0.002	18.231	0.002	18.631	0.002	20.036	0.004
SDSSJ130234.43+101238.9	16.191	0.002	16.522	0.002	17.036	0.002	17.514	0.002	17.903	0.001	19.302	0.004
SDSSJ131445.050-031415.588	18.258	0.004	18.600	0.005	19.106	0.004	19.572	0.004	19.936	0.008	21.327	0.008
SDSSJ151421.27+004752.8	15.112	0.002	15.390	0.002	15.708	0.002	16.119	0.002	16.470	0.001	17.783	0.004
SDSSJ155745.40+554609.7	16.501	0.002	16.877	0.002	17.472	0.002	17.991	0.002	18.389	0.002	19.832	0.005
SDSSJ163800.360+004717.822	18.013	0.007	18.321	0.004	18.842	0.004	19.285	0.003	19.663	0.004	21.002	0.007
SDSSJ172135.97+294016.0	20.374	0.013	20.089	0.012	19.666	0.005	19.670	0.003	19.769	0.003	20.551	0.024
SDSSJ181424.075+785403.048	15.792	0.002	16.122	0.002	16.543	0.002	17.005	0.002	17.392	0.001	18.783	0.002
SDSSJ203722.169-051302.964	18.262	0.004	18.549	0.004	18.947	0.005	19.377	0.003	19.677	0.005	20.981	0.020
SDSSJ210150.65-054550.9	18.075	0.003	18.337	0.003	18.655	0.003	19.063	0.002	19.419	0.003	20.741	0.006
SDSSJ232941.330+001107.755	17.947	0.004	18.110	0.004	18.161	0.004	18.473	0.003	18.784	0.004	19.993	0.006
SDSSJ235144.29+375542.6	17.456	0.003	17.666	0.003	18.074	0.002	18.461	0.002	18.790	0.002	20.069	0.004
					ILAPH							
Offsets			-0.033	0.003	-0.009	0.004	-0.014	0.002	0.009	0.004	-0.012	0.005
G191B2B	10.490	0.001	10.890	0.001	11.499	0.001	12.031	0.001	12.451	0.001	13.885	0.002
GD71	11.989	0.001	12.336	0.001	12.799	0.001	13.279	0.001	13.672	0.001	15.068	0.002
GD153	12.201	0.002	12.568	0.001	13.100	0.002	13.598	0.001	14.002	0.001	15.414	0.002
SDSSJ010322.19-002047.7	18.195	0.004	18.527	0.005	19.083	0.005	19.569	0.005	19.965	0.006	21.355	0.012
SDSSJ022817.16-082716.4	19.518	0.008	19.715	0.010	19.815	0.007	20.169	0.007	20.501	0.006	21.737	0.017
SDSSJ024854.96+334548.3	17.828	0.003	18.040	0.006	18.370	0.003	18.746	0.002	19.077	0.002	20.340	0.006
SDSSJ041053.632-063027.580	18.116	0.009	18.404	0.004	18.879	0.005	19.254	0.003	19.393	0.005	19.498	0.005
WD0554-165	16.776	0.005	17.153	0.003	17.727	0.005	18.220	0.002	18.617	0.005	20.043	0.007
SDSSJ072752.76+321416.1	17.163	0.003	17.471	0.003	17.993	0.003	18.457	0.002	18.837	0.003	20.217	0.007
SDSSJ081508.78+073145.7	18.950	0.006	19.263	0.008	19.716	0.005	20.184	0.005	20.579	0.006	21.962	0.024
SDSSJ102430.93-003207.0	18.261	0.018	18.514	0.004	18.904	0.004	19.317	0.004	19.665	0.010	20.990	0.013
SDSSJ111059.42-170954.2	17.041	0.003	17.354	0.004	17.867	0.003	18.313	0.002	18.689	0.002	20.057	0.005
SDSSJ111127.30+395628.0	17.443	0.004	17.830	0.006	18.420	0.003	18.939	0.004	19.344	0.002	20.797	0.009
SDSSJ120650.504+020143.810	18.240	0.004	18.489	0.004	18.672	0.004	19.060	0.003	19.411	0.007	20.703	0.008
SDSSJ121405.11+453818.5	16.940	0.002	17.283	0.002	17.761	0.002	18.236	0.003	18.629	0.002	20.038	0.004
SDSSJ130234.43+101238.9	16.188	0.002	16.522	0.002	17.036	0.002	17.514	0.002	17.904	0.002	19.303	0.004
SDSSJ131445.050-031415.588	18.258	0.004	18.597	0.005	19.102	0.005	19.567	0.005	19.955	0.009	21.328	0.012
SDSSJ151421.27+004752.8	15.110	0.002	15.391	0.002	15.709	0.002	16.120	0.002	16.471	0.001	17.787	0.004
SDSSJ155745.40+554609.7	16.500	0.002	16.877	0.002	17.470	0.003	17.992	0.002	18.388	0.002	19.834	0.005
SDSSJ163800.360+004717.822	18.016	0.007	18.318	0.004	18.840	0.005	19.281	0.003	19.660	0.005	20.996	0.009
SDSSJ172135.97+294016.0	20.371	0.013	20.078	0.015	19.656	0.004	19.670	0.003	19.768	0.003	20.552	0.021
SDSSJ181424.075+785403.048	15.791	0.002	16.121	0.002	16.544	0.002	17.001	0.002	17.393	0.001	18.786	0.002
SDSSJ203722.169-051302.964	18.257	0.007	18.544	0.004	18.943	0.006	19.350	0.012	19.672	0.010	20.979	0.023
SDSSJ210150.65-054550.9	18.068	0.004	18.334	0.004	18.656	0.003	19.064	0.002	19.414	0.004	20.740	0.008
SDSSJ232941.330+001107.755	17.943	0.004	18.109	0.004	18.161	0.006	18.470	0.003	18.775	0.007	19.995	0.006
SDSSJ235144.29+375542.6	17.449	0.004	17.662	0.003	18.075	0.003	18.459	0.003	18.787	0.002	20.075	0.004

Note. Photometry performed with three different software packages (i.e., DAOPHOT, Source Extractor and ILAPH) and the applied magnitude offsets between HST Cycle 20 and Cycle 22, as derived from Figure 9, are listed. See text for more details.

(This table is available in machine-readable form.)

CALSPEC standards obtained by using the three different software packages: DAOPHOT, SExtractor and ILAPH. The magnitudes have an average dispersion in the range 1-3 millimag for WFC3-UVIS filters and 5-10 milli-mag for the F160W IR filter. Machine readable photometry is available in Table 9.

Synthetic magnitudes in different photometric systems, such as PS, GAIA, and SDSS, for the set of standard DAWDs will be calculated and provided in NA19.

This study was supported by NASA through grants GO-12967 and GO-13711 from the National Optical Astronomy Observatory, which is operated by AURA, Inc., and grant GO-15113 from the Space Telescope Science Institute, which is operated by AURA, Inc., under NASA contract NAS 5-26555. E.O. was also partially supported by the NSF through grants AST-1313006 and AST-1815767. This work has made use of data from the European Space Agency (ESA) mission Gaia (https://www.cosmos.esa.int/gaia), processed by the Gaia Data Processing and Analysis Consortium (DPAC, https:// www.cosmos.esa.int/web/gaia/dpac/consortium). Funding for the DPAC has been provided by national institutions, particularly the institutions participating in the Gaia Multilateral Agreement.

Facilities: HST (WFC3), GEMINI, GAIA, Pan-STARRS.

Appendix

We provide here Table 10, which contains a list and descriptions of all the acronyms used in the manuscript.

Table 10 List of Acronyms used in the Manuscript, Grouped by Class and in Alphabetical Order

Acronym	Meaning
	Instruments/Detectors
ACS	Advanced Camera for Surveys
GALEX	Galaxy Evolution Explorer
GMOS	Gemini Multi-Object Spectrograph
HST	Hubble Space Telescope
LCO	Las Cumbres Observatory
LSST	Large Synoptic Survey Telescope
MMT	Multiple Mirror Telescope
MSX	Midcourse Space Experiment
STIS	Space Telescope Imaging spectrograph
UVIS1/2	Chips of the Wide-Field Camera 3 detector
WFC3-IR	Wide-Field Camera 3 Infrared detector
WFC3-UVIS	Wide-Field Camera 3 Ultraviolet and VISual detector
WISE	Wide-field Infrared Survey Explorer
	Surveys
ASAS-SN	All Sky Automated Survey for SuperNovae
ATLAS	Asteroid Terrestrial-impact Last Alert System
DES	Dark Energy Survey
PS	Pan-STARSS
SDSS	Sloan Digital Sky Survey
ZTF	Zwicky Transient Factory
	Software packages
ALLFRAME	Routine to perform simultaneous point-spread function photometry on different images (Stetson 1994)
DAOPHOT	DAOPHOTIV group of routines to perform aperture and point-spread function photometry (Stetson 1987)

Table 10 (Continued)

Acronym	Meaning
Drizzle Pac	Software to stack images collected with <i>Hubble Space</i> Telescope
ILAPH	IDL routines to perform aperture photometry from Abhijit Saha
SExtractor	Source Extractor software to perform aperture and point- spread function photometry (Bertin & Arnouts 1996)
	Others
AS	Artificial star
cal_wf3	Image calibration pipeline for the Wide-Field Camera 3 detectors
CALSPEC	Database of the <i>Hubble Space Telescope</i> spectro- photometric standard stars
CTE	Charge transfer efficiency
CR	Cosmic ray
CRNL	Count-rate nonlinearity
DAWD	Hydrogen atmosphere white dwarf
FoV	Field of view
FLUXCORR	Image header keyword indicating if the flux scaling needs to be performed
FWHM	Full-width half maximum
IMPHTTAB	Image photometry reference table
IR-FIX	Fixed aperture centered on the Wide-Field Camera 3 Infrared detector
IRSUB256-FIX	256×256 pixel sub-aperture on the center of the Wide-Field Camera 3 Infrared detector
IRSUB512-FIX	512 × 512 pixel sub-aperture on the center of the Wide- Field Camera 3 Infrared detector
MODTRAN	MODerate resolution atmospheric TRANsmission
NIR	Near-infrared
PAM	Pixel area map
PHOTFLAM	Image header keyword for the inverse sensitivity
PSF	Point-spread function
SED	Spectral energy distribution
UV	Ultraviolet
UVIS1-FIX	Fixed aperture centered on the UVIS1 chip of the Wide- Field Camera 3 Ultraviolet and VISual detector
UVIS2-	512×512 pixel sub-aperture on the corner of the
C512C-SUB	UVIS2 chip of the Wide-Field Camera 3 Ultraviolet and VISual detector
ZP	Zero-point

ORCID iDs

Annalisa Calamida https://orcid.org/0000-0002-0882-7702 Thomas Matheson https://orcid.org/0000-0001-6685-0479 Abhijit Saha https://orcid.org/0000-0002-6839-4881 Gautham Narayan https://orcid.org/0000-0001-6022-0484 Tim Axelrod https://orcid.org/0000-0002-5722-7199 Ralph Bohlin https://orcid.org/0000-0001-9806-0551 Christopher W. Stubbs https://orcid.org/0000-0003-0347-1724

Susana Deustua https://orcid.org/0000-0003-2823-360X Elena Sabbi https://orcid.org/0000-0003-2954-7643

References

Adelman-McCarthy, J. K., Agüeros, M. A., Allam, S. S., et al. 2008, ApJS, Bertin, E., & Arnouts, S. 1996, A&AS, 117, 393 Betoule, M., Kessler, R., Guy, J., et al. 2014, A&A, 568, A22

```
Bohlin, R. C. 2000, AJ, 120, 437
Bohlin, R. C. 2007, in ASP Conf. Ser. 364, The Future of Photometric,
   Spectrophotometric and Polarimetric Standardization, ed. C. Sterken (San
   Francisco, CA: ASP), 315
Bohlin, R. C. 2014, AJ, 147, 127
Bohlin, R. C., Colina, L., & Finley, D. S. 1995, AJ, 110, 1316
Bohlin, R. C., & Gilliland, R. L. 2004, AJ, 127, 3508
Bohlin, R. C., Gordon, K. D., & Tremblay, P.-E. 2014, PASP, 126, 711
Brinkworth, C. S., Burleigh, M. R., Lawrie, K., Marsh, T. R., & Knigge, C.
Brinkworth, C. S., Burleigh, M. R., Wynn, G. A., & Marsh, T. R. 2004,
         AS, 348, L33
Burke, D. L., Saha, A., Claver, J., et al. 2014, AJ, 147, 19
Chambers, K. C., Magnier, E. A., Metcalfe, N., et al. 2016, arXiv:1612.05560
Deustua, S. E., Mack, J., Bajaj, V., & Khandrika, H. 2017, WFC3/UVIS
   Updated 2017 Chip-dependent Inverse Sensitivity Values, Tech. Rep. ISR
   WFC3-2017-14
Deustua, S. E., Mack, J., Bowers, A. S., et al. 2016, UVIS 2.0 Chip-dependent
   Inverse Sensitivity Values, Tech. Rep. ISR WFC3-2016-03
Dupuis, J., Chayer, P., Vennes, S., Christian, D. J., & Kruk, J. W. 2000, ApJ,
   537, 977
Filippenko, A. V. 1982, PASP, 94, 715
Flewelling, H. A., Magnier, E. A., Chambers, K. C., et al. 2016, arXiv:1612.
Fontaine, G., & Brassard, P. 2008, PASP, 120, 1043
Fukugita, M., Ichikawa, T., Gunn, J. E., et al. 1996, AJ, 111, 1748
```

Gaia Collaboration, Brown, A. G. A., Vallenari, A., et al. 2018, A&A, 616, 1 Gennaro, M., Bajaj, V., & Long, K. 2018, A characterization of persistence at

short times in the WFC3/IR detector, Tech. Rep. ISR WFC3-2018-05

Hayes, D. S., Pasinetti, L. E., & Philip, A. G. D. (ed.) 1985, IAU Symp. 111,

Hermes, J. J., Gänsicke, B. T., Gentile Fusillo, N. P., et al. 2017, MNRAS,

Hilbert, B. 2009, WFC3 SMOV Program 11427: UVIS Channel Shutter

Hook, I. M., Jørgensen, I., Allington-Smith, J. R., et al. 2004, PASP, 116, 425

Calibration of Fundamental Stellar Quantities (Dordrecht: Reidel)

Holberg, J. B., Bergeron, P., & Gianninas, A. 2008, AJ, 135, 1239

Gianninas, A., Bergeron, P., & Ruiz, M. T. 2011, ApJ, 743, 138 Girven, J., Steeghs, D., Heber, U., et al. 2012, MNRAS, 425, 1013 Gorecki, A., Abate, A., Ansari, R., et al. 2014, A&A, 561, A128

Shading, Tech. Rep. ISR WFC3-2009-25

Holberg, J. B., & Bergeron, P. 2006, AJ, 132, 1221

Holberg, J. B., & Howell, S. B. 2011, AJ, 142, 62

468, 1946

```
Long, K. S., Wheeler, T., & Bushouse, H. 2011, IR Detector Timing and
  Persistence, Tech. Rep. ISR WFC3-2011-09
Massey, P., & Gronwall, C. 1990, ApJ, 358, 344
Massey, P., Strobel, K., Barnes, J. V., & Anderson, E. 1988, ApJ, 328, 315
Matheson, T., Kirshner, R. P., Challis, P., et al. 2008, AJ, 135, 1598
McCook, G. P., & Sion, E. M. 1999, ApJS, 121, 1
Narayan, G., Axelrod, T., Holberg, J. B., et al. 2016, ApJ, 822, 67
Narayan, G., Matheson, T., Saha, A., et al. 2019, ApJS, in press (arXiv:1811.
   12534)
Oke, J. B. 1974, ApJS, 27, 21
Oke, J. B., & Gunn, J. E. 1983, ApJ, 266, 713
Rauch, T., Werner, K., Bohlin, R., & Kruk, J. W. 2013, A&A, 560, A106
Riess, A. G. 2010, First On-orbit Measurements of the WFC3-IR Count-rate
   NonLinearity, Tech. Rep. ISR WFC3-2010-07
Riess, A. G. 2011, An Independent Determination of WFC3-IR Zeropoints and
  Count Rate NonLinearity from 2MASS Asterisms, Tech. Rep. ISR WFC3-
Riess, A. G., & Petro, L. 2010, Boosting Count-rates with Earth Limb Light
  and the WFC3/IR Count-rate Nonlinearity, Tech. Rep. ISR WFC3-2010-15
Sabbi, E. 2009, WFC3 SMOV Program 11798: UVIS PSF Core Modulation,
  Tech. Rep. ISR WFC3-2009-20
Sahu, K., Baggett, S., & MacKenty, J. 2014, Use of the Shutter Blade Side for
UVIS Short Exposures, Tech. Rep. ISR WFC3-2014-09
Sahu, K., Gosmeyer, C. M., & Baggett, S. 2015, WFC3/UVIS Shutter
  Characterization, Tech. Rep. ISR WFC3-2015-12
Schmidt, G. D., Weymann, R. J., & Foltz, C. B. 1989, PASP, 101, 713
Scolnic, D., Casertano, S., Riess, A., et al. 2015, ApJ, 815, 117
Shanahan, C. E., Gosmeyer, C. M., & Baggett, S. 2017, 2017 Update on the
   WFC3/UVIS Stability and Contamination Monitor, Tech. Rep. ISR WFC3-
  2017-15
Stetson, P. B. 1987, PASP, 99, 191
Stetson, P. B. 1994, PASP, 106, 250
Stone, R. P. S. 1977, ApJ, 218, 767
Stubbs, C. W., & Brown, Y. J. 2015, MPLA, 30, 1530030
Welch, D. L., & Stetson, P. B. 1993, AJ, 105, 1813
```

Khandrika, H., Deustua, S., & Mack, J. 2018, WFC3/UVIS-Temporal and

Long, K. S., Baggett, S., & MacKenty, J. W. 2013, Characterizing Persistence

in the WFC3 Channel: Observations of Omega Cen, Tech. Rep. ISR WFC3-

Spatial Variations in Photometry, Tech. Rep. ISR WFC3-2018-16

Kleinman, S. J., Kepler, S. O., Koester, D., et al. 2013, ApJS, 204, 5

Horne, K. 1986, PASP, 98, 609

2013-07